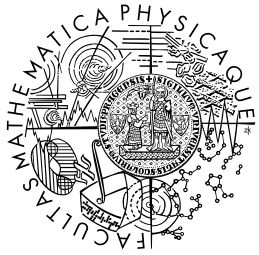

FACULTY
OF MATHEMATICS
AND PHYSICS
Charles University

BACHELOR THESIS

Matěj Dvořák

Reconstruction of ultrafast spin currents using terahertz spectroscopy

Department of Chemical Physics and Optics

Supervisor of the bachelor thesis: RNDr. Lukáš Nádvorník, Ph.D.

Study programme: Physics

Prague 2024

I declare that I carried out this bachelor thesis on my own, and only with the cited sources, literature and other professional sources. I understand that my work relates to the rights and obligations under the Act No. 121/2000 Sb., the Copyright Act, as amended, in particular the fact that the Charles University has the right to conclude a license agreement on the use of this work as a school work pursuant to Section 60 subsection 1 of the Copyright Act.

In ..... date ....

Author's signature

Most of all, I thank my supervisor, RNDr. Lukáš Nádvorník, Ph.D., both for his technical advice and for encouraging me whenever I thought everything was going wrong. When I was starting work on this bachelor thesis, I had not realised how vital a role the thesis advisor plays and how important his advice would be in directing me away from blind alleys and supporting me in well-directed efforts. I am thankful for Dr. Nádvorník's good judgment, without which this work could not exist. He has also been most accommodating to the occasional disruptions that my study this year has taken, mainly caused by applications for study abroad (which he has also helped me with very much). It is only thanks to his prompt responses that this work got finished before the deadline.

I thank my consultant Mgr. Jiří Jechumtál for introducing me to the laboratory and for his support regarding the experimental half of the work, Mgr. Zdeněk Kašpar, Ph.D. for supervising me for additional measurements on very short notice, and other members of the Laboratory of Terahertz Spintronics for discussions during our seminar.

Thanks is also due to prof. Tobias Kampfrath of Freie Universität Berlin, whose scripts formed the basis of the numerical half of this work.

Finally, I thank my family and friends for keeping me sane, both during the writing of this thesis and for all of my life before it.

Title: Reconstruction of ultrafast spin currents using terahertz spectroscopy

Author: Matěj Dvořák

Department: Department of Chemical Physics and Optics

Supervisor: RNDr. Lukáš Nádvorník, Ph.D., Department of Chemical Physics and Optics

Abstract: We describe a method by which it is possible to find the dynamics of a spin current in a spintronic terahertz emitter or other emitters derived from it. This method takes an experimental emission measurement from time-domain terahertz spectroscopy and removes the effects of the experimental setup, providing direct access to studying phenomena in the emitter. We implement it by simulating the process of optical rectification in a nonlinear crystal and measuring reference signals for a variety of emitters and setups. The transfer functions thus obtained for different emitters have good agreement among themselves and with theory, though the process is sensitive to the crystal refractive index. We then use the transfer function to reconstruct the dynamics of spin currents in two spintronic emitters, finding good agreement with previous measurements. We can discern multiple stages of the current dynamics: a sharp rise and fall, a dip into negative values and a slow relaxation. For further measurements, we recommend the use of thin crystals as references and detectors and the use of a dry air atmosphere, and we provide a Python script that automates the method.

Keywords: spin current, time-domain terahertz spectroscopy, ultrafast spintronics, transfer function

Název práce: Rekonstrukce ultrarychlých spinových proudů pomocí terahertzové spektroskopie

Autor: Matěj Dvořák

Katedra: Katedra chemické fyziky a optiky

Vedoucí bakalářské práce: RNDr. Lukáš Nádvorník, Ph.D., Katedra chemické fyziky a optiky

Abstrakt: V předložené práci popisujeme metodu, pomocí níž je možné určit dynamiku spinového proudu ve spintronickém emitoru. Metoda funguje tak, že odstraní vliv detekční aparatury na změřený emisní signál z terahertzové spektroskopie v časové doméně, čímž získáme přístup přímo k jevům probíhajícím v emitoru. Implementujeme ji simulací procesu optického usměrnění v nelineárním krystalu a měřením referenčních signálů pro řadu různých emitorů a experimentálních uspořádání. Přenosové funkce systémů, které takto získáme, jsou v dobré shodě jak mezi sebou, tak s teoretickým očekáváním. Proces je citlivý na index lomu použitého referenčního nelineárního krystalu. Přenosovou funkci dále používáme k rekonstrukci dynamiky spinových proudů ve dvou spintronických emitorech. Získané výsledky tvoří replikaci výsledků získaných skupinou ve Svobodné univerzitě v Berlíně. V získané dynamice lze rozlišit několik fází: prudký nárůst a pokles, propad do záporných hodnot, a pomalá relaxace. Pro další měření doporučejeme využití suché atmosféry a tenkých referenčních i detekčních krystalů. Výstupem práce je také program v Pythonu automatizující metodu rekonstrukce.

Klíčová slova: spinový proud, terahertzová spektroskopie v časové doméně, ultrarychlá spintronika, přenosová funkce

Contents

Introduction

Spintronics is a currently expanding field that promises faster and denser information technology devices, especially memory disks [1]. It uses the electron spin in addition to its charge, leading to the concept of a *spin current*, which may exist independently of a *charge current*.

Spintronics is already used in read heads of magnetic hard drives and in MRAM (magnetoresistive random-access memory), a nonvolatile, energy-saving memory device [2].

One of the possible eventual benefits of spintronics over conventional electronics is a greatly increased operating speed reached when combined with antiferromagnets, thanks to the faster spin manipulation possible in them compared to ferromagnets [3, 4]. This requires understanding spintronic processes at the corresponding terahertz frequencies and picosecond timescales. This task is approachable with the help of *terahertz (THz) spectroscopy in the time domain*. This technique can also help understand spin current dynamics on a fundamental level, for example, explaining spin current transfer across various types of interfaces.

The ultimate goal of this thesis is to measure the dynamics of a spin current in a *spintronic terahertz emitter* (STE), as detailed in chapter 1. Our method is measuring the THz pulse emitted by the STE, finding the transfer function of the detection setup, and performing a numerical deconvolution. To find the transfer function, we need a theoretical understanding of THz emission from nonlinear crystals through difference-frequency generation, including factors affecting the emission such as phase-matching, reflections, and Fresnel losses at interfaces (chapter 2). We then implement the analytical models into a numeric script and generate the theoretical emission pulses from the crystals used (chapter 3). We then measure the actual emission signals (chapter 4), apply the numeric method to extract the transfer function, and use it to reconstruct spin current dynamics in multiple samples (chapter 5). We conclude by discussing the optimal experimental procedure for using this method and avenues for further work (chapter 6).

Our goals are to:

- Measure the signals from several nonlinear crystals under multiple experimental conditions.
- Find the transfer function for each setup, verifying that different emitters provide consistent results.
- Compare the experimentally determined transfer function with theoretical expectations.
- Reconstruct the temporal dynamics of a spintronic emitter. Determine the level of detail the present experimental equipment can reach.
- Automate the process of spin current reconstruction for the purposes of future experiments.

1 Motivation

1.1 Terahertz spectroscopy

Spectroscopy is the study of material properties and processes through their interaction with light [5]. Different light must be used for different processes depending on their energy and/or time scales. THz radiation is particularly well suited to processes on time scales of approximately picoseconds, as $1\,\mathrm{ps} = (1\,\mathrm{THz})^{-1}$ [6, 7]. Ref. [8] provides an introduction into the experimental techniques and fundamental concepts.

THz radiation lies in the so-called "terahertz gap" between infrared optical spectroscopy and high-frequency electronic measurements, see figure 1.1. This spectral range was inaccessible to experiments for a long time because of a lack of usable sources and detectors [7]. This was a problem as many solid-state excitation phenomena (such as phonons, magnons, or charge carrier scattering on impurities) lie in this frequency range. The development of femtosecond lasers has opened this area to experimental study. Among the applications are noninvasive imaging for medical, security, or quality control purposes [7] or studying the vibrational modes of biomolecules [6].

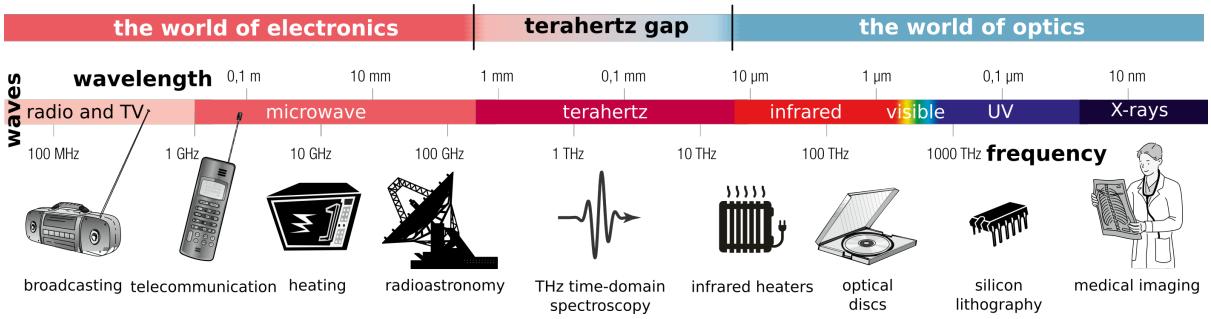

Figure 1.1 THz radiation in the light spectrum. Image reproduced from [9].

Time-domain terahertz spectroscopy is a spectroscopic technique that can, unlike conventional spectroscopy, record not only the intensity of light, but also its phase; i.e., it allows us to reconstruct the temporal dependence of the electric field, the *THz waveform* [7]. This allows us in principle to reconstruct the time profile of the underlying charge and spin currents.

1.2 Ultrafast spin currents

Our work was done in the context of the research projects of the Laboratory of THz Spintronics[1]. A recent motivating overview of the laboratory's research area and its applications is [9].

One important application of time-domain THz spectroscopy is the study of the dynamics of ultrafast (picosecond-scale and faster) processes, such as ultrafast spin currents in spintronics. This is the application this work approaches.

[1] https://www.mff.cuni.cz/en/kchfo/ooe/laboratories/thz

By *spintronics* we mean the use of spin degrees of freedom of electrons in information processing technology [10]. This allows, among other things, storing information in antiferromagnetic materials, rather than the traditionally used ferromagnetic ones [4, 11]. That has advantages in both access and switching speed (which could thus move from the gigahertz range to the terahertz range) and in memory density, as antiferromagnetic bits don't affect neighboring bits nearly as much as ferromagnetic ones. Ref. [3] provides a review of the use of THz radiation for reading and writing data in antiferromagnetically oriented materials.

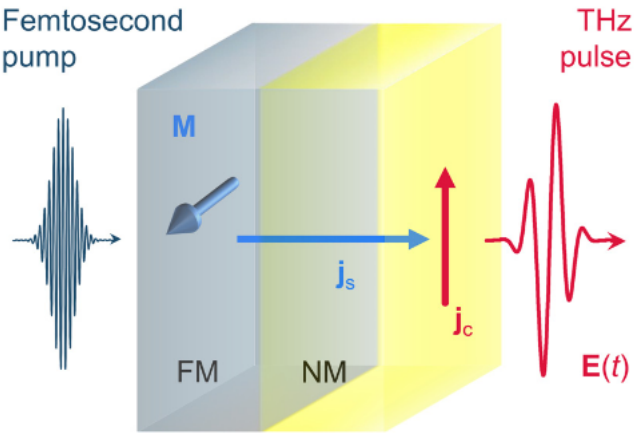

Figure 1.2 An illustration of the mechanism of spintronic emitters for the case of a bilayer. Reproduced from [12]. The bilayer consists of a ferromagnetic layer (FM) with a magnetization $\vec{M}$ induced by a permanent magnet on top of the emitter and a non-ferromagnetic metal (NM), typically a heavy metal such as platinum. An optical femtosecond pulse arrives from the left. It excites electrons in the FM layer and creates a current j_s from the FM into the NM. Since it originates in a magnetized material, this current is spin-polarized in the direction of $\vec{M}$. This process is called *spin current injection*. Within the NM layer, the spin current is converted through the *inverse Spin Hall effect* into a perpendicular charge current j_c. This transient current emits THz dipole radiation.

An *ultrafast spin current* is a current of charged particles (typically electrons) whose spin points in a common direction [13]. It can be, for example, very efficiently generated in a *spintronic THz emitter* (STE). A simple case to explain the principle is a bilayer spintronic emitter, illustrated in figure 1.2. It consists of two nanometer-scale metallic layers, the first a ferromagnet, the second a heavy metal, placed in an external magnetic field from a permanent magnet [12, 14, 15]. An incoming optical pulse creates a charge current from the ferromagnet into the heavy metal. The current is spin-polarized, because all its electrons started out with their spins oriented parallel to the magnetization of the ferromagnet. Within the heavy metal, the *inverse spin Hall effect* converts the out-of-plane spin current to an in-plane charge-current [16]. This current emits dipole radiation, with the electric field at the exit face of the bilayer related to the charge current density j through the metal conductivity σ:

$$E = \frac{j}{\sigma} \tag{1.1}$$

A common case for metals for $\Omega < 3\,\mathrm{THz}$ is that $\sigma(\Omega)$ is frequency-independent [17], so knowing the temporal dynamics of $E(t)$ would also tell us about the dynamics $j(t)$ of the

current itself. This would let us study the dynamics of $j(t)$ originated in STE samples with more complex interfaces as well.

1.3 Spin current reconstruction

In time-domain THz spectroscopy, we measure the dependence of the electric field amplitude of a THz pulse on time [6, 7]. However, the signal $S(t)$ we measure is not directly the electric field $E(t)$ that was produced in the emitter (so called "near field"). It is affected by propagation through the setup (forming the "far field") and the sensitivity of the detection method. Reconstructing the original signal requires a combination of experiment and modeling [18, 19, 20, 21].

Fortunately, the experiment is linear in that the electric field does not interact with itself. This mathematically means that the relationship between the electric field $E(t)$ just behind the sample and the measured signal $S(t)$ in the detector is captured by a convolution:

$$S(t) = E(t) * h(t) \tag{1.2}$$

The function $h(t)$, called the *transfer function*, is determined by the experimental setup. It represents the detection response to a hypothetical Dirac δ-pulse; the convolution represents the adding up of such responses for a general shape of $E(t)$. If we know $h(t)$, we can invert equation 1.2 and find the electric-field shape $E(t)$ from the measured signal $S(t)$.

We may attempt to calculate $h(t)$ from theory [6, 7, 22], but that would require a complete characterization of the setup, which is a complicated procedure that has to be repeated for any change in the setup. It is simpler to avoid documenting the experimental setup explicitly and instead do it implicitly, by performing a reference measurement with an emitter whose true $E(t)$ we know.

For inverting (1.2), it is more convenient to work in the frequency domain, that is, to perform a Fourier transform [23], which we define (for any temporal waveform $f(t)$) as:

$$f(\omega) = \int_{-\infty}^{\infty} f(t) e^{-i\omega t} \, \mathrm{d}t \tag{1.3}$$

Its inverse is:

$$f(t) = \int_{-\infty}^{\infty} f(\omega) e^{i\omega t} \, \mathrm{d}\omega \tag{1.4}$$

The Fourier transform turns the convolution into a multiplication:

$$S(\omega) = E(\omega) h(\omega) \tag{1.5}$$

From (1.5), it is obvious that on knowing two out of S, E, and h, we can find the third. The process used in this thesis is this: we measure a reference signal S_{ref} from a well-known emitter and the signal S out of an unknown (specifically, spintronic) emitter,

under conditions that differ as little as possible[2]. We calculate E_{ref} based on theoretical considerations, then use E_{ref} and S_{ref} to calculate h, then use h to go from S to E. All together this is represented by equations (1.6) and (1.7):

$$h(\omega) = \frac{S_{ref}(\omega)}{E_{ref}(\omega)} \tag{1.6}$$

$$E(\omega) = S(\omega)\frac{E_{ref}(\omega)}{S_{ref}(\omega)} \tag{1.7}$$

In this thesis, we use ZnTe (zinc telluride) and GaP (gallium phosphide) nonlinear crystals as reference emitters to reconstruct the current dynamics in spintronic emitters (STE).

[2]Ideally, the only change between the measurements is exchanging one emitter for the other, though in the case of measurements in dry air, it is necessary to wait for the air to re-dry.

2 Modeling generation of THz radiation

In this chapter we describe how to calculate the modeled $E(t)$ emitted from a nonlinear crystal after an excitation by an ultrafast laser pulse.

First, we describe laser pulses and note the two separate orders of magnitude of frequencies used: near infrared and THz.

Second, we describe the process of *difference-frequency generation* (DFG) for a pair of monochromatic waves. We work step by step: first we find electric polarization produced by DFG, then we find the electric field produced by that polarization in an infinitesimal crystal slice, then we integrate over the crystal length.

Third, we find the effects of interface transmission and reflection on incoming and outcoming radiation.

Finally, we integrate the formula for monochromatic waves from the second step over the spectrum obtained in the third step.

2.1 Laser pulses

A pulse laser outputs light over a frequency range that depends on the pulse duration. This is crucial for a quantitative understanding of THz radiation generation.

We may equivalently describe the output of a pulse laser through its electric field amplitude in time $E(t)$ or in angular frequency $E(\omega)$. The relationship between these two descriptions is the Fourier transform, as described in equations (1.3) and (1.4).

We can use this formalism to describe a Gaussian wave packet. Its spectrum is defined in [6][1] to be:

$$E(\omega) = \frac{E_0}{2\sqrt{\pi}\sqrt{\Gamma}} \exp\left(\frac{-(\omega-\omega_0)^2}{4\Gamma}\right) \tag{2.1}$$

The inverse Fourier transform of this spectrum yields the time domain description:

$$E(t) = \frac{E_0}{2\sqrt{\pi}\sqrt{\Gamma}} e^{i\omega_0 t} e^{-\Gamma t^2} \tag{2.2}$$

E_0 can be interpreted as the peak electric intensity (thanks to the normalization factors). Γ is a parameter describing the frequency bandwidth.

In both descriptions, there is a Gaussian pulse with a characteristic size at which E drops to $\frac{1}{e}E_0$. We denote these sizes by $\Delta\omega = 2\sqrt{\Gamma}$ and $\Delta t = \frac{1}{\sqrt{\Gamma}}$. These relations hold for transform-limited laser pulses.

[1] We have added the normalization factors that E_0 is divided by to give E_0 a meaning: the peak field amplitude.

Δt is related to τ, the FWHM[2] duration of the pulse, through a factor of $2\sqrt{\ln 2}$:

$$\Delta t = \frac{\tau}{2\sqrt{\ln 2}} \tag{2.3}$$

There is an analogical relation between the spot FWHM radius ρ and w_0, the beam waist parameter.

We can find E_0 from the pulse energy W, which follows from the excitation power P_{exc} and the laser repetition rate f_{rep}:

$$W = \frac{P_{exc}}{f_{rep}} \tag{2.4}$$

Assuming a Gaussian beam in both space and time, we find peak intensity I_0 as:

$$I_0 = \frac{W}{\pi^{\frac{3}{2}} \Delta t w_0^2} \tag{2.5}$$

Peak field amplitude is then (see for example [24]):

$$E_0 = \sqrt{\frac{2}{nc\varepsilon_0} I_0} \tag{2.6}$$

Our laser parameters are $\lambda_0 = 1030\,\text{nm}$ (central wavelength), $\tau = 170\,\text{fs}$, $\rho = 575\,\mu\text{m}$, $f_{rep} = 10\,\text{kHz}$. From this, we obtain $\omega_0 = 2\pi\frac{c}{\lambda_0}$, $\Gamma = \frac{1}{(\Delta t)^2}$, $w_0 = \frac{\rho}{2\sqrt{\ln 2}}$. The resulting spectrum is shown in figure 2.1.

[2]Full width at half maximum

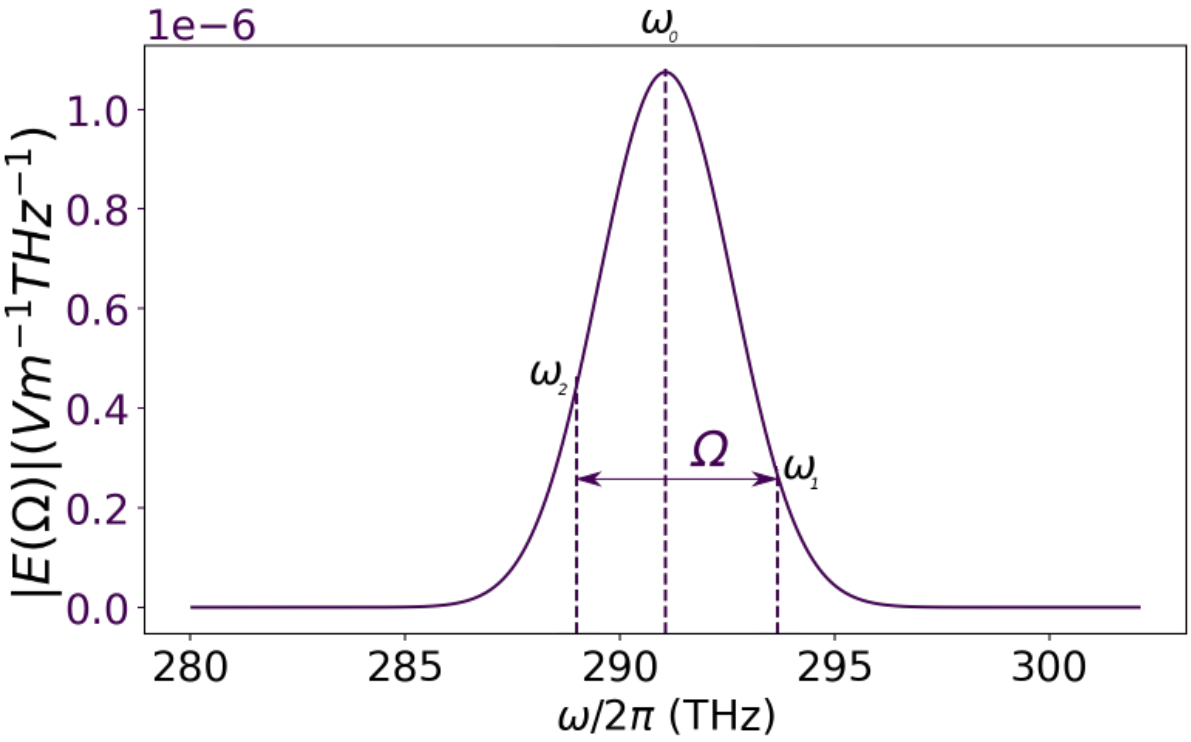

Figure 2.1 The spectrum of our laser with example frequencies taking part in the DFG. ω_0 is the central frequency, ω_1 the higher frequency, ω_2 the lower one, and $\Omega = \omega_1 - \omega_2$ is produced by DFG.

We see that the spectrum is centered in the optical range, while its bandwidth is in the THz range. Throughout this entire thesis, ω is used for frequencies in the optical range (or for generic frequencies) and Ω for frequencies in the THz range.

2.2 Nonlinear crystals and difference-frequency generation

Nonlinear crystals are used both for the generation and the detection of THz radiation. The underlying principle that makes them useful for these purposes is a nonlinear relationship between the electric field E and electric polarization P. We define the electric susceptibility χ using the vacuum permittivity ε_0 as:

$$P(E) = \varepsilon_0 \chi(E) E \tag{2.7}$$

The nonlinear dependence of P on E becomes significant only at strong fields, so we can expand it into a Taylor series:

$$P(E) = \varepsilon_0 \sum_{i=1}^{\infty} \chi_{(i)} E^i \tag{2.8}$$

The generation of THz radiation uses *difference-frequency generation*[3] (DFG), while its

[3]The term *optical rectification* is also sometimes used.

detection uses *the Pockels effect* [6, 7]. Both of these are consequences of a nonzero $\chi_{(2)}$ term present in noncentrosymmetric materials, so we neglect higher-order terms and only consider the term P_2:

$$P_2 = \varepsilon_0 \chi_{(2)} E^2 \tag{2.9}$$

Now, let's illustrate the principle on a toy model: Let us have two monochromatic electromagnetic waves with different frequencies, $E_1(t) = E_1 \cos \omega_1 t$ and $E_2(t) = E_2 \cos \omega_2 t$. The second-order term in polarization gives us:

$$P_2(t) = \varepsilon_0 \chi_{(2)} [E_1(t) + E_2(t)]^2 = \varepsilon_0 \chi_{(2)} [E_1^2(t) + E_2^2(t) + 2E_1(t)E_2(t)] \tag{2.10}$$

The squared terms can be rewritten thanks to the identity $\cos^2 x = \frac{1+\cos 2x}{2}$ as the generation of the second harmonic and the production of a constant polarization, which are effects irrelevant for our purposes. We only consider the term mixing E_1 and E_2:

$$P_{mix}(t) = 2\varepsilon_0 \chi_{(2)} E_1(t) E_2(t) = 2\varepsilon_0 \chi_{(2)} E_1 E_2 \cos \omega_1 t \cos \omega_2 t \tag{2.11}$$

Using a trigonometric identity, we find:

$$P_{mix}(t) = \varepsilon_0 \chi_{(2)} E_1 E_2 \left[\cos(\omega_1 + \omega_2)t + \cos(\omega_1 - \omega_2)t\right] \tag{2.12}$$

Thus we get terms in the polarization that oscillate at the sum and difference frequencies. The sum-frequency term is again irrelevant for our purposes.

$$P_{DFG}(t) = \varepsilon_0 \chi_{(2)} E_1 E_2 \cos(\omega_1 - \omega_2)t \tag{2.13}$$

The difference-frequency term is what allows us to generate THz radiation. For ω_1 and ω_2 with a difference on the order of the pulse bandwidth, i.e., $\omega_1 - \omega_2 = \Omega$, P_{DFG} has a component oscillating at frequency Ω (see figure 2.1). Thus, THz frequency generation is possible given a laser with a bandwidth of at least a few THz, i.e., a pulse laser with sufficiently short pulses.

2.2.1 Complex-wave formalism

As we use the Fourier transform, which is built on the complex exponential, it is convenient to find the analogous result in the complex-wave formalism [25]. That is, we consider a sinusoidal wave with amplitude E_0 the real part of a complex wave with complex amplitude $\widetilde{E}_0$:

$$E_0 \sin(\omega t) = \frac{1}{2}(\widetilde{E}_0 e^{i\omega t} + \widetilde{E}_0^* e^{-i\omega t}) \tag{2.14}$$

We then identify E_0 and $\widetilde{E}_0$, implicitly taking the real part when interpreting quantities as physically meaningful. We begin with equation (2.11). Inserting the complex representation from equation (2.14), we get:

$$P_{mix}(t) = \frac{1}{2}\varepsilon_0\chi_{(2)}[\widetilde{E}_1\widetilde{E}_2 e^{i(\omega_1+\omega_2)t} + \widetilde{E}_1\widetilde{E}_2^* e^{i(\omega_1-\omega_2)t} + \widetilde{E}_1^*\widetilde{E}_2 e^{i(\omega_2-\omega_1)t} + \widetilde{E}_1^*\widetilde{E}_2^* e^{-i(\omega_1+\omega_2)t}] \tag{2.15}$$

The terms with frequency $\pm(\omega_1 + \omega_2)$ are again irrelevant for our purposes, leaving:

$$P_{DFG}(t) = \frac{1}{2}\varepsilon_0\chi_{(2)}[\widetilde{E}_1\widetilde{E}_2^* e^{i(\omega_1-\omega_2)t} + \widetilde{E}_1^*\widetilde{E}_2 e^{i(\omega_2-\omega_1)t}] \tag{2.16}$$

We find that this is the representation of a complex polarization wave:

$$\widetilde{P}_{DFG}(t) = \varepsilon_0\chi_{(2)}\widetilde{E}_1\widetilde{E}_2^* e^{i(\omega_1-\omega_2)t} \tag{2.17}$$

2.3 Reflection and transmission on interfaces

Both incoming optical radiation and outgoing THz radiation are affected by reflection and transmission at the interfaces between the crystal and air. [26] This is captured by Fresnel's formulae (t_{AB} being the amplitude transmission coefficient for light going from material A to material B):

$$t_{AB} = \frac{2n_A}{n_A + n_B} \tag{2.18}$$

$$r_{AB} = \frac{n_B - n_A}{n_A + n_B} \tag{2.19}$$

We define t_{in} by setting $n_A = 1$ (air) and $n_B = n(\omega)$ (crystal), t_{out} by setting $n_A = n(\omega)$ (crystal) and $n_B = 1$ (air), and r_{in} and r_{out} analogously.

There is also the possibility of multiple reflections. They are represented by a factor $M(\omega)$:

$$M(\omega) = \sum_{n=0}^{\infty}[r_{out}^2(\omega)e^{2iLk_B(\omega)}]^n = \frac{1}{1 - r_{out}^2(\omega)e^{2iLk_B(\omega)}} \tag{2.20}$$

The effect of multiple reflections is optional, since the reflections produce pulses delayed by the time it takes the optical pulse to travel $2L$. Even for the thinnest crystal we use, which is ZnTe with $L = 100\,\mu\text{m}$, this delay is $n\frac{2L}{c} \approx 2\,\text{ps}$, which is longer than the pulse itself, so we can cut the reflections off (see section 3.5 for illustrations). Thus, we set $M = 1$.

To get the field actually in the crystal, we need $t_{in}(\omega)$ and $M(\omega)$. We denote by $E_c(\omega)$ the electric field in the crystal at frequency ω.

$$E_c(\omega) = E_{inc}(\omega)t_{in}(\omega)M(\omega) \tag{2.21}$$

E_{inc} is given by formula (2.1).

2.4 Dipole radiation

2.4.1 Green's function

To get from P_{DFG} to E_{DFG} at the end of the crystal[4], we apply the formula for dipole radiation from [18] to an infinitesimal slice of the crystal at coordinate z:

$$\mathrm{d}E = -2\pi \frac{1}{\varepsilon_0 c^2} \frac{\exp[ik(L-z)]}{k} \frac{\partial^2}{\partial t^2} \mathrm{d}P \tag{2.22}$$

L is the crystal thickness, z the coordinate within the crystal, k is the spatial frequency of the THz radiation in the crystal ($k = \frac{\Omega}{c} n(\Omega)$).

In the frequency domain, the second derivative in time simply yields a factor of Ω^2.

$$\mathrm{d}E(\Omega) = -2\pi \frac{\Omega^2}{\varepsilon_0 c^2} \frac{\exp[ik(L-z)]}{k} \mathrm{d}P \tag{2.23}$$

We insert P_{DFG} from (2.17), assume that $\chi_{(2)}(\omega - \Omega) \approx \chi_{(2)}(\omega)$ (see formula (3.4) in section 3.2), and get:

$$\mathrm{d}E(\Omega) = -2\pi \chi_{(2)} E(\omega) E^*(\omega - \Omega) \frac{\Omega}{nc} \exp[ik(L-z)] \mathrm{d}z \tag{2.24}$$

2.4.2 Phase mismatch

THz radiation is generated throughout the crystal along its length L. This is important because of dispersion: the refractive index of the crystal depends strongly on frequency, which means that THz radiation generated at different z coordinates will reach the end of the crystal with a different phase. [26]

To describe this effect quantitatively, we use the spatial frequency k. The phase of the outgoing THz radiation depends on the coordinate z where its conversion took place. Let us have two optical frequencies ω and $\omega - \Omega$ that travel together for a length z, then convert through DFG into radiation at frequency Ω, then travel the remaining length $L - z$ as THz radiation.

This is represented by a contribution to the integral (2.24). The complex phase of this $\mathrm{d}E$ also depends on the phases of the two incoming pulses: $\phi(\omega, z) = k(\omega)z$ and $\phi(\omega - \Omega, z) = k(\omega - \Omega)z$. Because of the complex conjugation, the polarization phase is:

$$\phi_P(z) = \phi(\omega, z) - \phi(\omega - \Omega, z) \tag{2.25}$$

The resulting THz dipole radiation is emitted in both directions: forwards along the crystal and backwards. Since a part of the backwards-emitted radiation reflects off the crystal end, we must also consider its contribution. [26] The phase of the outgoing radiation is then:

[4] Still within the crystal, i.e., before transmission through the interface.

$$\phi(z) = [k(\omega) - k(\omega - \Omega)]z \pm (L - z)k(\Omega) \tag{2.26}$$

with the $\pm$ depending on whether the radiation is emitted forwards (+) or backwards (-). We can introduce the *phase mismatch spatial frequency* $\Delta k_\pm$:

$$\Delta k_\pm = k(\omega) - k(\omega - \Omega) \pm k(\Omega) \tag{2.27}$$

Because of the negative sign in equation (2.26), Δk_- corresponds to forward emission, while Δk_+ corresponds to backward emission.

To find only the phase mismatch factor, we integrate the phase component of (2.24), replacing k with $\Delta k_\pm$, over the crystal thickness L. We thus get the phase mismatch factor $\psi(\Omega, \omega)$:

$$\psi(\Omega, \omega) = e^{ik(\Omega)L} \int_0^L e^{iz\Delta k_-} + r_{out}(\Omega) e^{iz\Delta k_+} \, \mathrm{d}z \tag{2.28}$$

This integral has an analytic solution:

$$\psi(\Omega, \omega) = e^{ik(\Omega)L} \left(\frac{e^{iL\Delta k_-} - 1}{\Delta k_-} + r_{out}(\Omega) \frac{e^{iL\Delta k_+} - 1}{\Delta k_+} \right) \tag{2.29}$$

Combined with the prefactors in formula (2.24), we get the total outgoing $E(\Omega)$:

$$E(\Omega, \omega) = -2\pi\chi_{(2)} \frac{\Omega}{cn(\Omega)} \psi(\Omega, \omega) E(\omega) E^*(\omega - \Omega) \tag{2.30}$$

2.5 THz reference emission formula

DFG converts a part of an optical pulse into radiation at frequencies comparable to the pulse bandwidth. A near-infrared laser beam is thus converted into the much longer-wave THz radiation, as anticipated in section 2.2 and equation (2.13).

In this section, we combine results from previous sections into a formula describing emission from the nonlinear crystals used in our experiments. We do this by integrating formula (2.30) over the field in the crystal from formula (2.21). We assume that $\chi_{(2)}(\Omega)$ is independent of ω (see section 3.2 for details).

We add together $E_c(\omega)$ from formula (2.21), $\psi(\Omega, \omega)$ from formula (2.29), $t_{out}(\Omega)$ from formula (2.18) and $M(\Omega)$ from formula (2.20). The emitted THz radiation is then:

$$E(\Omega) = \int_0^\infty E_c(\omega) E_c^*(\omega - \Omega) \psi(\Omega, \omega) t_{out}(\Omega) M(\Omega) \, \mathrm{d}\omega \tag{2.31}$$

We note that if we neglect $\psi(\Omega, \omega)$ and interface effects, this is the *autocorrelation function* $A(\Omega)$:

$$A(\Omega) = \int_0^\infty E_c(\omega) E_c^*(\omega - \Omega) \, \mathrm{d}\omega \tag{2.32}$$

2.6 Effects affecting the transfer function

In this section, we outline effects of the propagation of the THz radiation through the setup and its detection on the spectrum of the resulting transfer function.

2.6.1 Absorption on water vapor

Water molecules have absorption lines in the THz spectrum caused by transitions between rotational and vibrational states [6]. If the THz radiation passes through water vapor, parts of it get absorbed and, consequently, reemitted, leading to a jagged spectrum, as seen in figure 2.2, or delayed replicas of the pulse in the temporal domain. The same jagged spectrum and delayed replicas are thus to be expected in the transfer function.

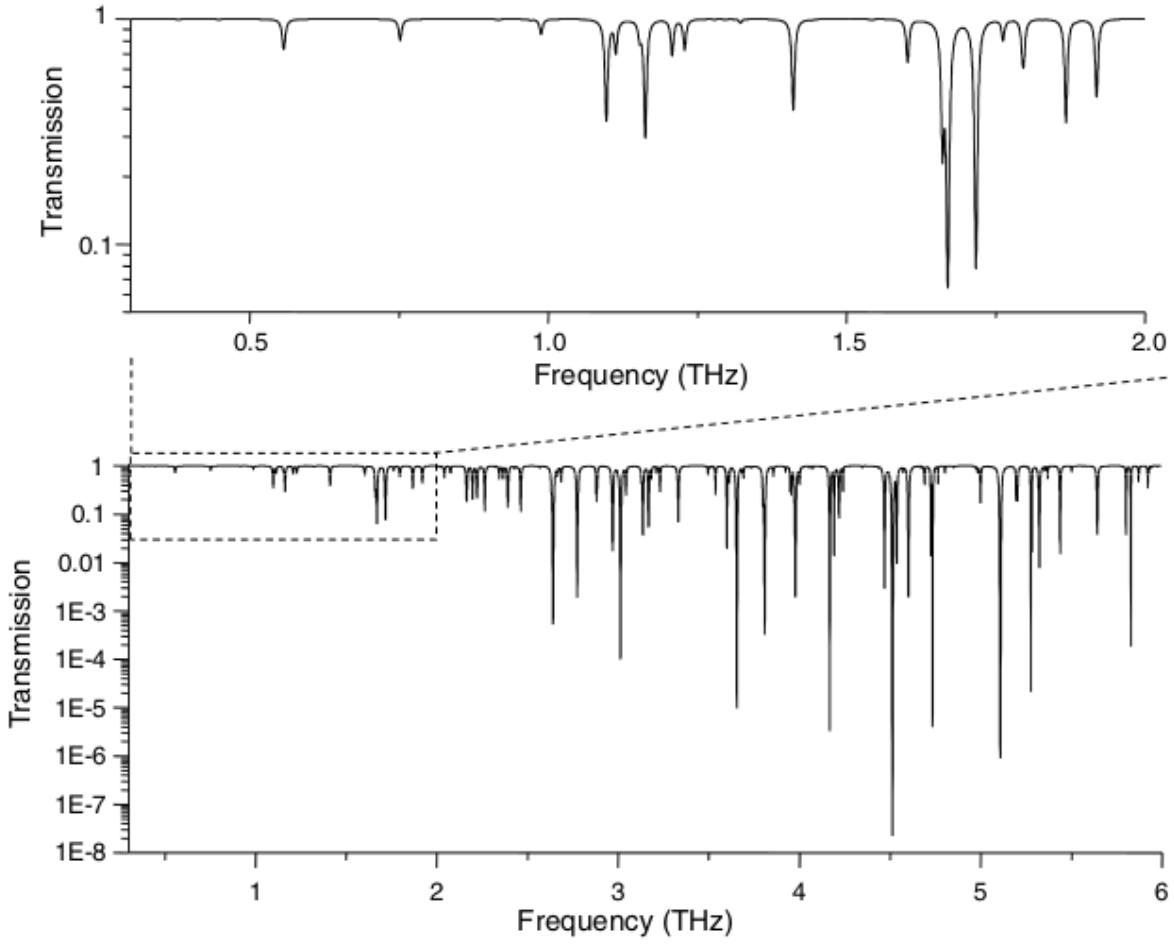

Figure 2.2 The transmission spectrum of water vapor. Image taken from [6].

2.6.2 Beam cutting at component apertures

THz radiation propagates as a Gaussian beam [7]. The divergence θ of such a beam depends on its wavelength as $\tan(\theta) = \frac{\lambda}{\pi w_0} = \frac{c}{2\Omega w_0}$ (w_0 being the Gaussian radius). Thus, lower frequencies have a greater θ and are more divergent. For very low Ω, θ is so large that the beam doesn't fit inside optical components (such as parabolic mirrors) and part of it is consequently lost. The effect of this is a high-pass filter in the transfer function.

2.6.3 Detection in a nonlinear crystal

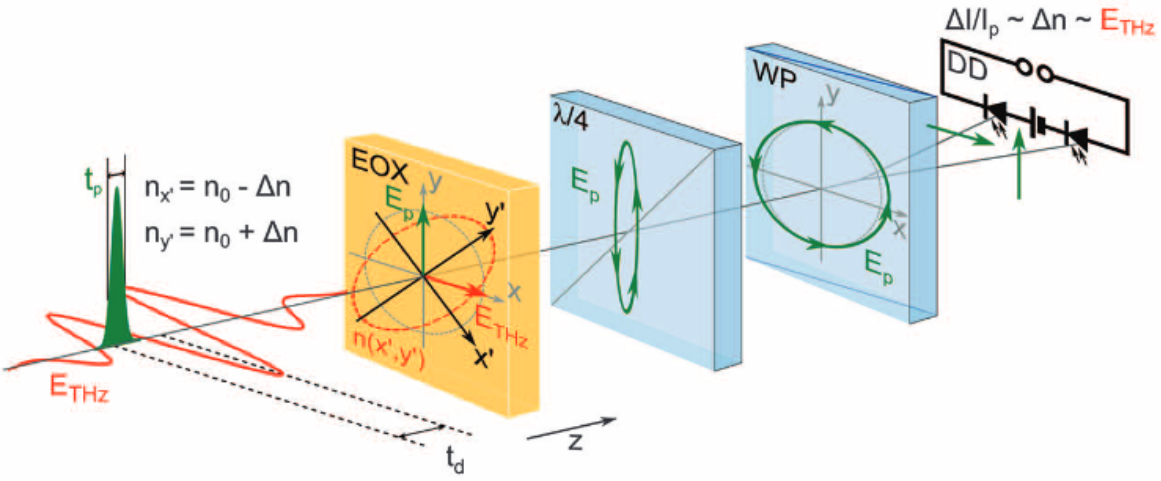

Figure 2.3 An illustration of electrooptic sampling. The THz (red curve) and optical (green area) pulses copropagate through a detection crystal (EOX). The optical pulse then passes through a quarter waveplate ($\lambda/4$) and a Wollaston prism (WP). A difference signal is read off two balanced photodiodes. Image taken from [27].

The detection of THz radiation is done through the process of *electrooptic (EO) sampling* [6, 7], illustrated on figure 2.3. Electrooptic sampling works thanks to the Pockels effect, which means that the crystal behaves as a general waveplate (i.e., it induces a phase shift between orthogonal polarization modes) in the presence of an external electric field. The role of the external field is played by the THz pulse, which is focused together with a detection optical pulse on the detection crystal. The THz wavelength is about 50 times the optical wavelength, so the THz field is nearly constant in the pulse area ($t_d \gg t_p$ in figure 2.3). Thus, it may be treated as a static field.

At the exit of the detection crystal, the linearly polarized optical pulse has acquired a certain degree of ellipticity. The quarter waveplate turns this polarization state into an almost circularly polarized state. The Wollaston prism separates two linear projections in the x and y directions. Due to the imperfect circular mode, their difference is nonzero, easy to measure, and directly proportional to the THz field amplitude. The part of the THz pulse that is being measured is selected through a time delay between the optical and THz pulse, controlled by a delay line in the setup.

THz detection and emission have the same underlying principle through the nonlinear susceptibility $\chi_{(2)}$ and a copropagation of THz and optical beams through a nonlinear crystal. The same phase-matching, autocorrelation and transmission and reflection terms apply in both emission and detection [28]. The sensitivity spectrum of a given crystal as a detector is thus comparable with its theoretical emission as an emitter.

3 Spin current reconstruction method

In this chapter, we show how the analytical model described in the previous chapter is implemented in a numeric script.

3.1 The numerics of the Fourier transform

We use the Discrete Fourier Transform (DFT) implemented in the NumPy package. DFT converts an array of N values, x_n, into another array of N values, X_n. We use the unitary definition with equal scaling in the forward and backward direction, as documented in the NumPy FFT (Fast Fourier Transform) module manual[1]:

$$X_n = \frac{1}{\sqrt{N}} \sum_{k=0}^{N-1} \exp\left(\pm 2\pi i k \frac{n}{N}\right) \tag{3.1}$$

The + sign is used in the forward transform, the − sign in the inverse transform.

DFT is a map between complex-valued functions. In general, it transforms real-valued functions into complex-valued ones. However, both $E(t)$ and $S(t)$ are related to physical values that are fundamentally real. We thus want $h(t)$ to also be a real-valued function.

The DFT of a real-valued function is Hermitian: $X_k = X^*_{N-k}$. When finding h for a given reference measurement, we select a frequency range where the measurement is reliable, calculate the theoretical emission, and find their ratio (1.6). This creates an array X_k that is not Hermitian, so we append its complex conjugate, getting an array of length $2N - 1$ (as the zero-frequency term is not duplicated):

$$X_{N+k} = X^*_{N-k} \tag{3.2}$$

This is equivalent to continuing the reconstruction into the negative frequencies.

3.2 Material parameters

The calculations in section 2.5 depend on the values of n and $\chi_{(2)}$ for GaP and ZnTe. These values are frequency-dependent; this dependency is expressed through empirical or theoretically motivated formulae.

Refractive indices in the THz range are modeled as Lorentzian oscillators [29]:

$$n(\Omega) = \sqrt{\varepsilon_\infty \left(1 + \frac{\Omega_{LO}^2 - \Omega_{TO}^2}{\Omega_{TO}^2 - \Omega^2 - i\gamma\Omega}\right)} \tag{3.3}$$

[1] https://numpy.org/doc/stable/reference/routines.fft.html#module-numpy.fft

Here, ε_∞ is the high-frequency dielectric constant, γ is the phonon damping rate, and Ω_{LO} and Ω_{TO} are the longitudinal and transverse optical phonon frequencies. The values of these constants are summed up in table 3.1 and the resulting function $n(\Omega)$ is shown in figure 3.1.

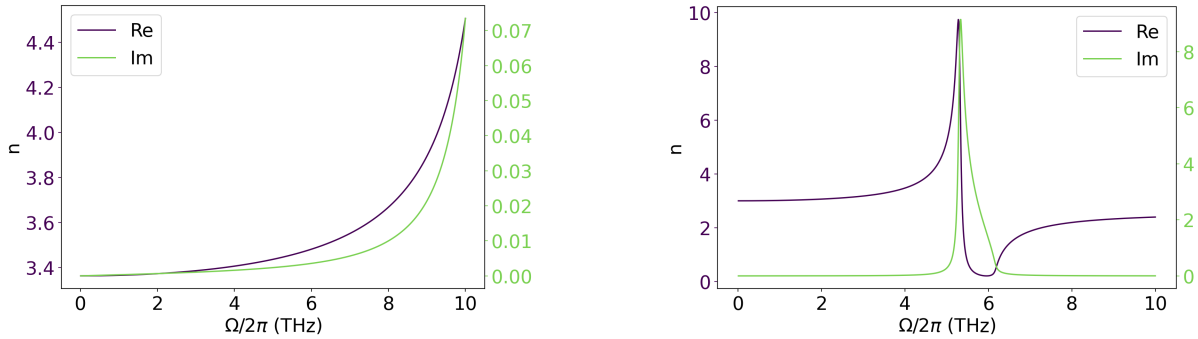

(a) GaP **(b)** ZnTe

Figure 3.1 Refractive indices in the THz range for (a) GaP and (b) ZnTe crystals. Panel (b) shows the overall frequency dependence with a divergence caused by absorption by phonons. However, our experimental bandwidth is limited to $0-4$ THz.

Using figure 3.1, we can show the effect of the various constants. ε_∞ is a multiplicative factor, Ω_{TO} specifies the location of the resonance where n diverges (see panel 3.1b), γ affects the width of this resonance, and Ω_{LO} affects the variability of n through $k_{TO} = \Omega_{LO}^2 - \Omega_{TO}^2$.

The divergence causes absorption of THz radiation generated around the frequency Ω_{TO}, causing problems when using nonlinear crystals for high THz frequency generation. Since our experimental bandwidth is limited to $0-4$ THz, we never reach this divergence and our results aren't affected by it very strongly. In particular, they are practically unaffected by changes in γ.

The dependence of $\chi_{(2)}(\Omega)$ is captured by equation (3.4):

$$\chi_{(2)}(\Omega) = \frac{n_{VIS}^4 r_{41}}{2(1+C_{FH})}\left(1 + C_{FH}\frac{\omega_{TO}^2}{\omega_{TO}^2 - \Omega^2 + i\gamma\Omega}\right) \tag{3.4}$$

The term on the left is the pure electronic coefficient given by [30], the term on the right comes from [29]. The formula as a whole comes from [18].

r_{41} is the electrooptic coefficient, n_{VIS} is the material refractive index at 632 nm, and C_{FH} is the Faust-Henry coefficient. The result is plotted in figure 3.2.

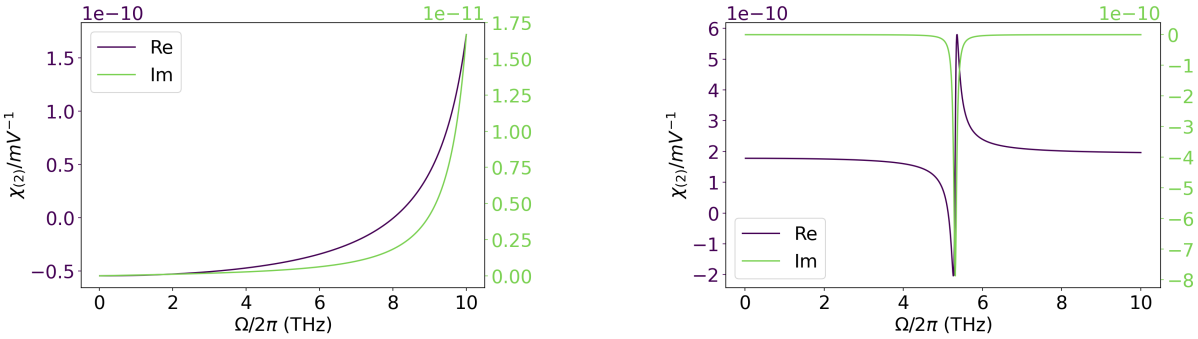

(a) GaP **(b)** ZnTe

Figure 3.2 The dependence of nonlinear susceptibility on the THz frequency for (a) GaP and (b) ZnTe crystals. Note the divergence in the same frequency range as the divergence of n, as seen in figure 3.1.

Material	ZnTe	GaP
ε_∞	6.7 [29]	9.65 [31]
$\Omega_{TO}2\pi$	5.31 THz [32]	11.01 THz [31]
$\frac{\Omega_{LO}}{2\pi}$	6.17 THz [32]	12.082 THz [31]
$\frac{\gamma}{2\pi}$	90.3 GHz [29]	129 GHz [29]
C_{FH}	-0.07 [29]	-0.47 [29]
r_{41}	$4.45 \times 10^{-12}\ \frac{\mathrm{m}}{\mathrm{V}}$ [33]	$-0.88 \times 10^{-12}\ \frac{\mathrm{m}}{\mathrm{V}}$ [30]

Table 3.1 Material constants

There is disagreement between sources over the value of γ. Gallot et al. [32] provides only an upper limit on $\frac{\gamma}{2\pi}$ for ZnTe of 25 GHz, which contradicts Leitenstorfer et al. [29], which puts the value at around 90 GHz. We use the latter value. As we cannot reach the divergence situated at Ω_{TO} with the laser bandwidth used, our results are not sensitive to the value of γ.

In the optical range, we use empirical formulae taken from [31] (GaP) and [34] (ZnTe) ($\lambda = \frac{2\pi c}{\Omega}$ being the wavelength in micrometers):

$$n_{ZnTe}(\omega) = \sqrt{4.27 + 3.01\frac{\lambda^2}{\lambda^2 - 0.142}} \tag{3.5}$$

$$n_{GaP}(\omega) = \sqrt{4.1705 + 4.9113\frac{\lambda^2}{\lambda^2 - 0.1174} + 1.9928\frac{\lambda^2}{\lambda^2 - 756.46}} \tag{3.6}$$

The frequency dependence $n(\omega)$ in the optical range for both crystals is plotted in figure 3.3.

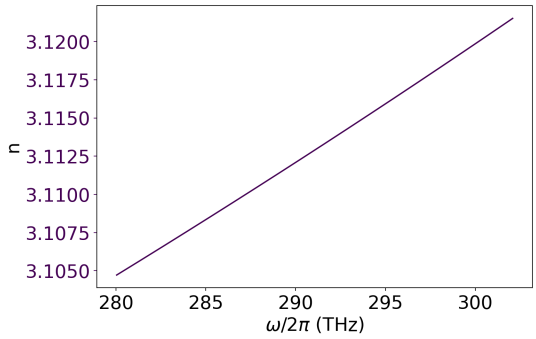

(a) GaP

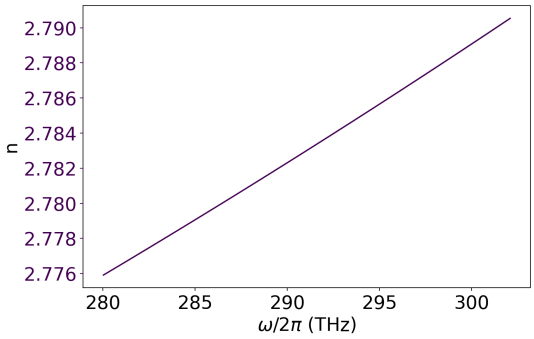

(b) ZnTe

Figure 3.3 Refractive indices of nonlinear crystals in the optical range.

3.3 Algorithmic implementation

For all data processing in this thesis, we have created an overarching Python script. The program builds upon multiple scripts in Matlab by prof. Tobias Kampfrath from Freie Universität Berlin implementing formula (2.31) for use in [18]. We have modified the scripts, adapting them to the different system parameters[2] and translating them from Matlab to Python. In addition to this theoretical core, we added a script for processing of our measured data through formula (1.7).

Our program accepts input in the form of a folder containing at least one subfolder. Each subfolder contains measurements made in a single setup. Measurements may be reference or unknown (in our case spintronic) emitter measurements. Each reference measurement file is named in a format that contains the crystal material, thickness, and excitation power used, which is enough to construct the reference emission spectrum using formula (2.31).

The script works in the following steps:

- For each reference, the raw data in the form of $S_{ref}(t)$ from the corresponding measurement file is Fourier-transformed into $S_{ref}(\Omega)$ through the FFT.
- $E_{ref}(\Omega)$ is calculated using the emission model (2.31) for the set of Ω values from the measured data. This is done for frequencies between 0 and 4 THz, as for higher frequencies, $S_{ref}(\Omega)$ is zero.
- $h(\Omega)$ is calculated using (1.6). This process is documented in a graph showing $E_{ref}(\Omega)$, $S_{ref}(\Omega)$, $h(\Omega)$ together for user convenience. The transfer functions calculated using different reference measurements in the same setup are plotted together as well.
- The transfer functions are transformed into the time domain $h(t)$ through the inverse FFT, aligned with the first pulse processed, then transformed back into $h(\Omega)$. This removes any shifts caused by different time windows between measurements.

[2]The main difference between the setups is in the optical laser parameters and crystal substrates. In addition, we have explicitly listed the parameters in table 3.1 and created procedures for their fitting, used in section 5.1.

- An average $h(\Omega)$ is calculated for each setup. Details of averaging are treated in section 3.4.2, complex numbers are treated by averaging the real and imaginary parts separately.
- The transfer functions are plotted in the time domain using the inverse FFT. Their average is plotted as well.
- For every measurement from an unknown (spintronic) emitter, $S(\Omega)$ is processed from the corresponding measurement file. The corresponding $E(\Omega)$ is calculated using the averaged $h(\Omega)$ from the previous step in formula (1.5). E is then plotted in the frequency and time domain.
- The average $h(\Omega)$ from different setups are plotted together for their comparison.

The integral in (2.31) is calculated numerically as a Riemann integral with 1000 bins. The integration domain of ω is $\omega_0 \pm 5\Delta\omega$ (as defined in section 2.1).

3.4 Handling uncertainties

3.4.1 Error sources

The data that we measure contains random noise. Thus, we perform every measurement with a time window containing data points before the THz waveform we want to measure, where we expect no signal. We take the standard deviation of the first 15 data points of each measurement to be the noise level. We assume that the error level is equal for all points in our data.

3.4.2 Averaging data with error bars

Let us have two measurements of a single value, A and B. Assuming both measurements are represented as normal distributions with expectation values μ_A and μ_B and standard deviations σ_A and σ_B, what can we say about the value from both measurements combined?

The product of the individual normal distributions is another normal distribution with a new μ and σ given by formulae [35]:

$$\mu = \frac{\mu_A \sigma_B^2 + \mu_B \sigma_A^2}{\sigma_A^2 + \sigma_B^2} \tag{3.7}$$

$$\sigma = \frac{\sigma_A \sigma_B}{\sqrt{\sigma_A^2 + \sigma_B^2}} \tag{3.8}$$

We will use this result to combine the transfer functions from different emitters into a single average for a given setup. When averaging multiple values, we can combine them in any order, as this operation is commutative and associative.

3.4.3 Error propagation through DFT

DFT is defined by the sum in equation (3.1). For normally distributed data, multiplication by a complex number of magnitude 1 doesn't affect the error, while the variance σ^2 of

a sum is the sum of the variances σ_i^2. Multiplication by the scalar $\frac{1}{\sqrt{N}}$ multiplies the variance by $\frac{1}{N}$, meaning that the variance of every point in the DFT output is the average variance of the transformed function [36]:

$$\sigma^2 = \frac{1}{N}\sum_{i=1}^{N}\sigma_i^2 \tag{3.9}$$

For the special case where the transformed function already has identical error at every data point, DFT has no effect on error size at all.

We note that even single points with great uncertainty, such as those where there is no emission expected, create a large uncertainty over the entire transform result. We avoid this effect by using multiple emitters. The weighted average (3.7) from the previous section then automatically discards data points with very large error bars.

3.5 Results: Reference emission data

Figure 3.4 shows both the reference emission data for various crystals we used and its sensitive dependency on the refractive index of the crystal for thick crystals. This is caused by the phase mismatch factor (2.26), which creates interference-caused minima whose position depends on n.

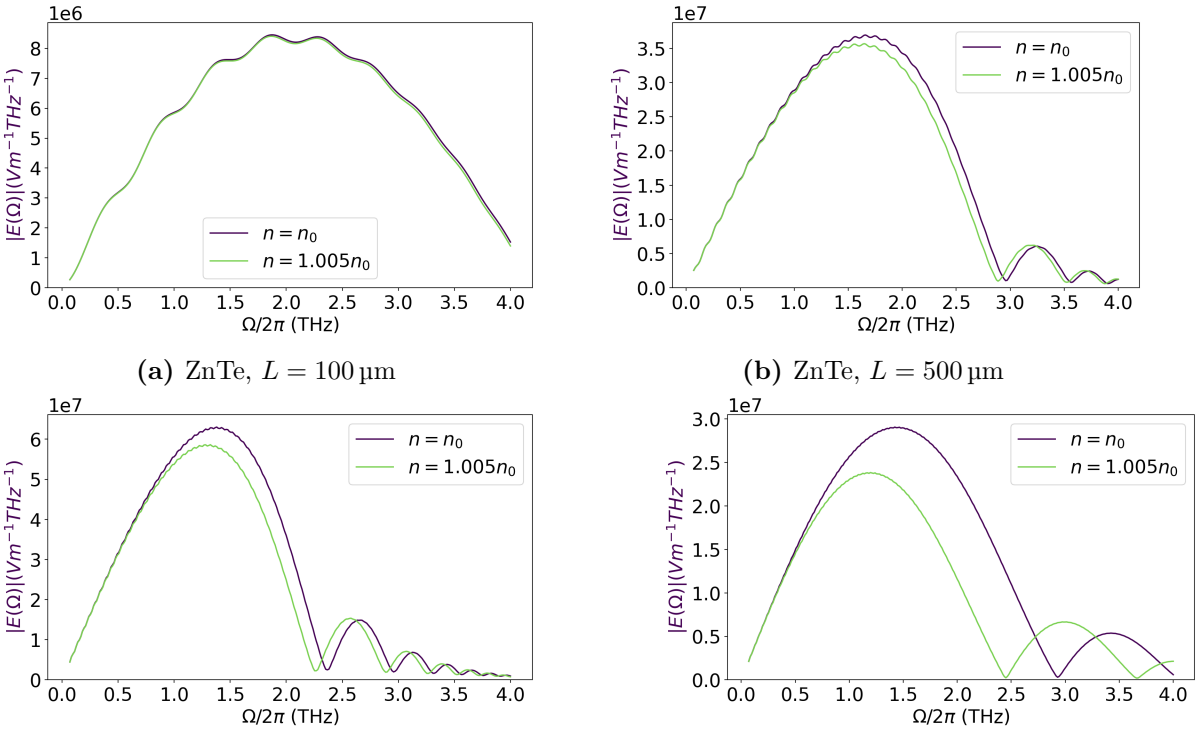

(a) ZnTe, $L = 100\,\mu m$

(b) ZnTe, $L = 500\,\mu m$

(c) ZnTe, $L = 1000\,\mu m$

(d) GaP, $L = 2000\,\mu m$

Figure 3.4 The reference emission spectrum from various crystals used in this work and its sensitivity to a change in n by 0.5%. For thick crystals, the uncertainty in n may cause major changes in the position of the minima, which may complicate the determination of the transfer function.

Because of the large sensitivity of the method to the crystal refractive index, small deviations between the theoretical values from table 3.1 and actual value have a significant impact on the accuracy of the method.

We also plot the reference waveforms (obtained through DFT of the theoretical spectrum for $n = n_0$) in figure 3.5. As the echoes are clearly distinguishable from the main pulse, we have not simulated them in further work.

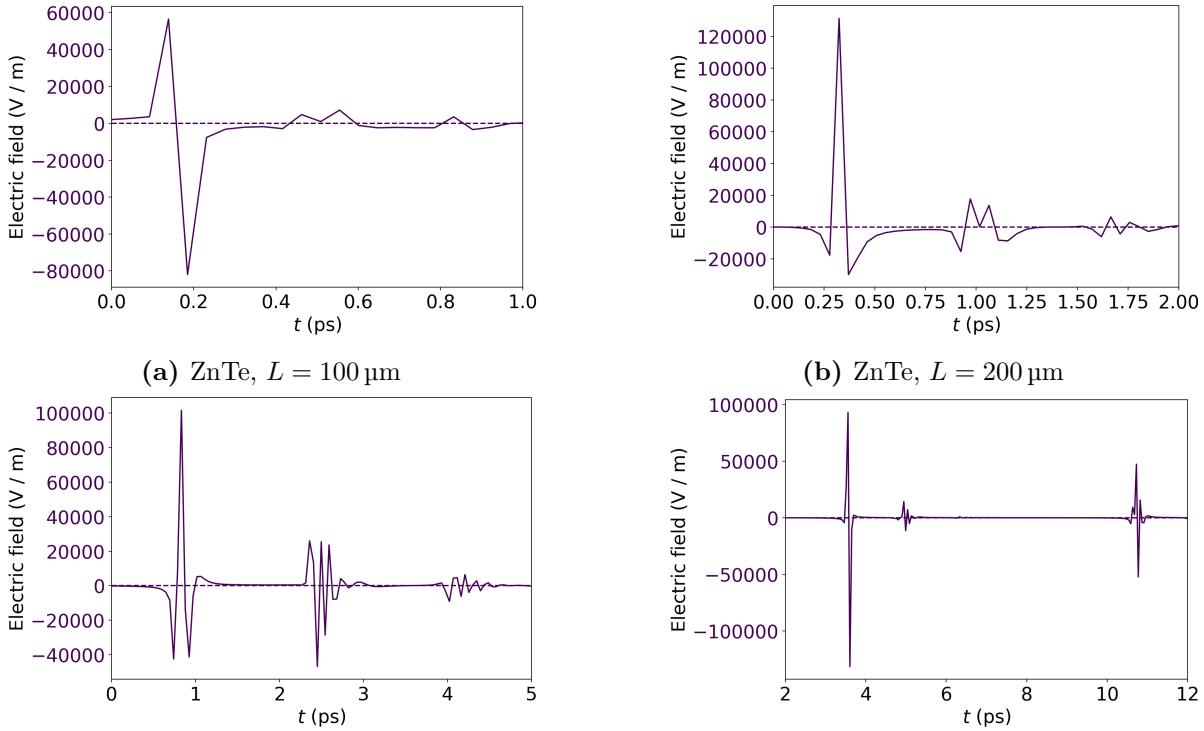

(a) ZnTe, $L = 100\,\mu\text{m}$

(b) ZnTe, $L = 200\,\mu\text{m}$

(c) ZnTe, $L = 500\,\mu\text{m}$

(d) GaP, $L = 2\,\text{mm}$

Figure 3.5 Theoretical emission in the time domain for various crystals. Note that even in the thinnest crystal in (a), the first echo is clearly distinct from the main pulse. Note also the increasing delay of both the main pulse and its echoes with increasing crystal thickness.

4 Experiments

4.1 Experimental setup

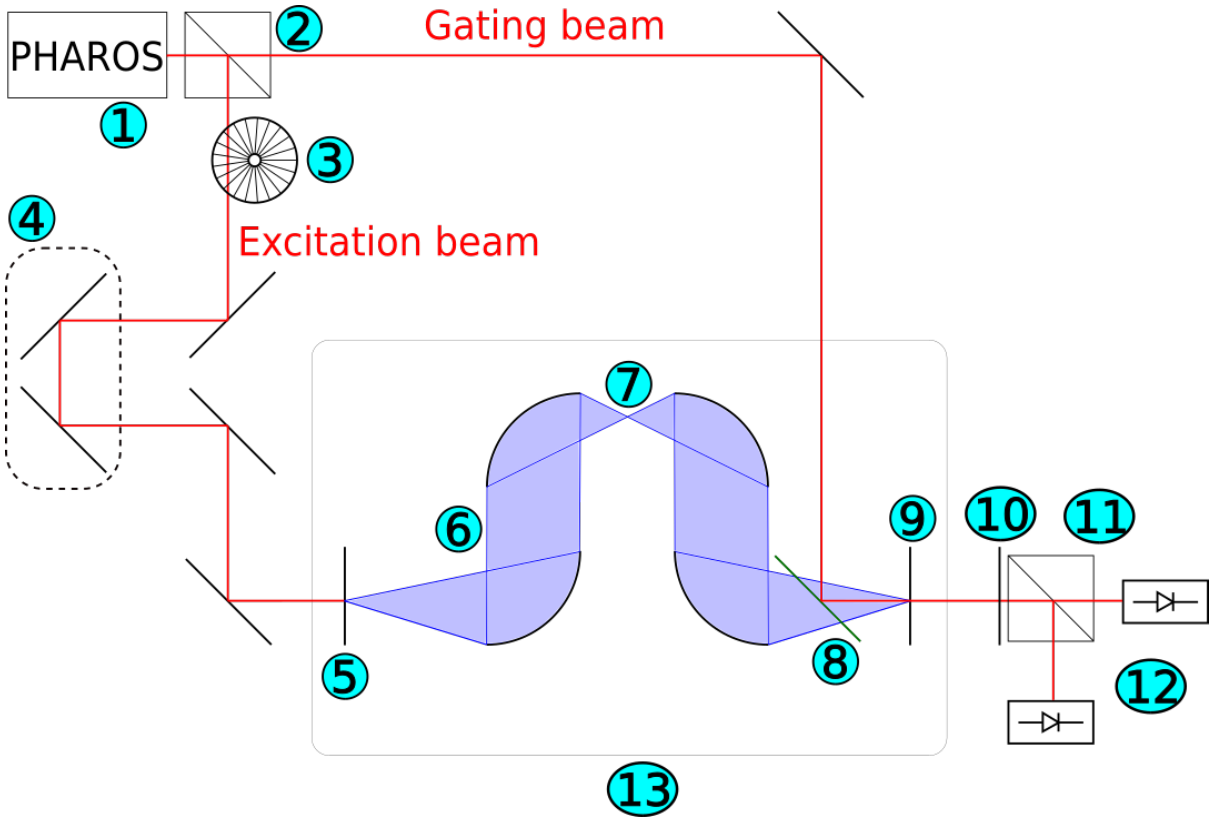

Figure 4.1 Our experimental setup. A PHAROS femtosecond laser (1) produces an optical pulse (shown in red). The pulse is divided (2) into an excitation and detection (also called *gating*) beam. The excitation beam passes through a mechanical chopper (3), a delay line (4) and is focused on the emitter (crystal or STE) (5), which emits pulses of divergent THz radiation (shown in blue). This radiation is first collimated by a parabolic mirror in the area (6), then focused into a sample area (7) by another parabolic mirror. After passing through the sample area, the beam diverges onto another parabolic mirror that collimates it again, then a final mirror that focuses it on the detection crystal (9). Here, it overlaps with the detection beam, which is incoupled using a pellicle beamsplitter (8). In the detection crystal, the optical beam gains a slight ellipticity. After passing through a quarter waveplate (10), the beam is split in a Wollaston prism (11), and the difference signal is measured on a pair of balanced photodiodes (12). The part of the setup where the THz radiation propagates can be optionally enclosed in a flowbox (13) connected to an air dryer and flooded with dry air. A hygrometer is used to verify that there are no leaks and humidity remains at 0%.

Our setup is illustrated on figure 4.1. The PHAROS laser (1) has central wavelength $\lambda_0 = 1030\,\text{nm}$, pulse FWHM duration $\tau = 170\,\text{fs}$, and set repetition rate $f_{rep} = 10\,\text{kHz}$. The power of the detection beam is 0.7 mW. The excitation beam's power depends on the emitter used, as described below in table 4.4. The chopper (3) rotates at a frequency around 1500 Hz (this occasionally requires modification to find a frequency that suppresses

the background setup noise well). The spot at (5) has FWHM diameter $\rho = 575\,\mu\text{m}$. The sample area (7) is used in transmission experiments; we left it empty.

Measurements that used the iris shutter (as explained below) were performed by adding the iris to the area (6) where THz radiation is collimated.

4.2 List of measurements

We have measured signals from a range of emitters using a range of detectors under various experimental conditions.

As detectors, we have used the following $\langle 110 \rangle$-oriented crystals of thickness L (and setup modifications):

- ZnTe, $L = 500\,\mu\text{m}$
- ZnTe, $L = 1\,\text{mm}$
- ZnTe, $L = 2\,\text{mm}$
- GaP, $L = 2\,\text{mm}$
- GaP, $L = 2\,\text{mm}$, in dry air
- GaP, $L = 2\,\text{mm}$, iris shutter in the collimated area at various diameters.

We have measured combinations of detectors and emitters. They are listed in table 4.1 with the measurement amplitudes[1]. Additionally, we have measured signals from 8 experimental emitters produced by Dr. Jakub Zázvorka (Institute of Physics, Charles University) with the GaP detector (without dry air), as described in table 4.2.

Finally, we measured the signal from the ZnTe 1 mm emitter using the GaP 2 mm detector, with the iris shutter set at various diameters. These measurements are summarized in table 4.3.

Emitter/Detector	GaP, dry air	GaP	ZnTe 500 µm	ZnTe 1 mm	ZnTe 2 mm
3-layer STE	34.3		2.93	9.4	5.2
2-layer STE	26.9	18.3	2		
ZnTe 100 µm	26.1	13.6	1.4		
ZnTe 200 µm	11.1	5.9	0.79		
ZnTe 500 µm	11.1	5.9	—		
ZnTe 1 mm	8	6.1	0.79	—	
ZnTe 2 mm	5	3.2	0.34		—
GaP 2 mm	—	—	16.7	61.2	

Table 4.1 Amplitudes ($S_{max} - S_{min}$) in mV. Each column corresponds to one setup.

[1] By *amplitude*, in this section, we mean the difference between the maximal and minimal value of $S(t)$.

Sample number	L (nm)	Amplitude (mV)
1	0	0.63
2	0.5	0.68
3	1	0.64
4	1.5	0.52
5	2	0.46
6	3	0.31
7	7	0.25
8	10	0.14
ZnTe 1 mm reference	—	6.10

Table 4.2 Amplitudes ($S_{max} - S_{min}$), experimental emitters

Iris diameter	Amplitude (mV)
1 cm	0.83
2 cm	2.2
3 cm	4.8
4 cm	5.9
5 cm (fully open)	6.0
No iris	6.1

Table 4.3 Amplitudes ($S_{max} - S_{min}$), the iris shutter at various diameters

4.3 Samples used

The regular spintronic emitters used were a bilayer CoFeB(2)/Pt(2) (*2-layer STE* from now on) and a trilayer W(2)/CoFeB(1.8)/Pt(2) (*3-layer STE* from now on) grown on a sapphire (Al_2O_3) substrate. The numbers in brackets are layer thicknesses in nm.

The experimental emitters we used were grown by sputtering. They consist of several layers on a silicon substrate: SiO_2(3)/Au(L)/Pt(5)/Co(2)/Au(5). The thickness L of the bottom Au layer is variable. As gold grows porously, it affects the roughness of the interface between the Pt/Co layers, which form a bilayer STE. The top layer of gold prevents oxidation.

The nonlinear crystals were bought from Eksma Optics (ZnTe)[2] and Swiss THz (GaP)[3].

[2]The data sheet is available at https://eksmaoptics.com/out/media/EKSMA_Optics_GaSe-ZnTE_Crystal.pdf

[3]https://www.swissterahertz.com/thz-detectivecrystals

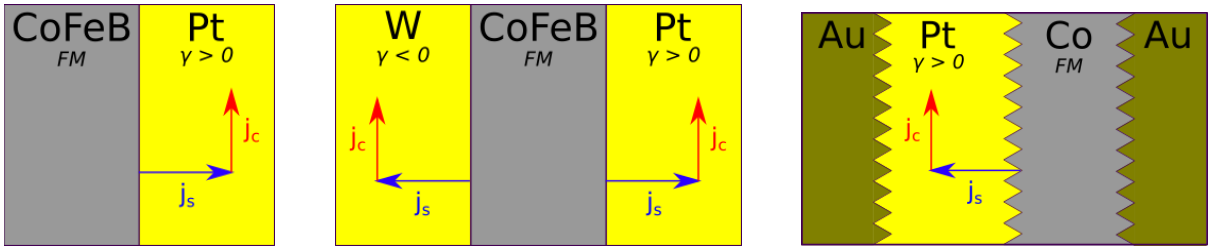

(a) (b) (c)

Figure 4.2 Illustrations of the spintronic emitters used. (a) A bilayer consisting of a ferromagnet and a heavy metal. (b) A trilayer. The ferromagnet is in the middle. Upon excitation by an optical pulse, spin-polarized currents enter two non-ferromagnetic metal layers. Thanks to the different signs of the spin Hall angle γ (a material parameter describing the strength of the spin Hall effect) in each metal, the induced charge currents are deflected in parallel directions and the emission is stronger. [14] (c) The experimental emitters. The gold layer on the left creates a rough interface between the different layers. The gold layer on the right is there only to prevent corrosion.

4.4 Experimental procedure

We performed measurements in batches, each batch with a single setup. Within each batch, we periodically exchanged various emitters. Between batches, we exchanged the detector and possibly changed the experimental conditions (adding or removing dry air and/or the iris shutter). With each emitter, we started at a low excitation power (around 2 mW), gradually increased it and observed the amplitude. When the amplitude started to reach saturation (that is, it no longer rose linearly with the excitation power), we noted the excitation power and performed the measurement itself at this maximal allowed power. Figure 4.3 shows a representative saturation curve. The excitation powers used for each emitter are listed in table 4.4.

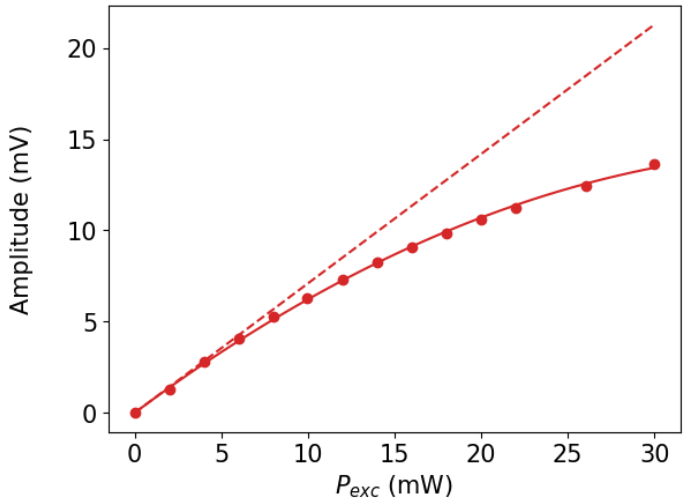

Figure 4.3 Example saturation curve for the ZnTe 100 µm emitter, measured with the GaP detector without dry air. The dashed line extrapolates the linear regime. The value of P_{exc} used for this emitter is 30 mW, at which point the saturation losses are 36%.

Emitter	P_{exc} (mW)
3-layer spintronic emitter	16
2-layer spintronic emitter	18
ZnTe, $L = 100\,\mu m$	30
ZnTe, $L = 200\,\mu m$	12
ZnTe, $L = 500\,\mu m$	10
ZnTe, $L = 1\,mm$	6
ZnTe, $L = 2\,mm$	7
GaP, $L = 2\,mm$	40
Experimental emitters	16

Table 4.4 Emitters and excitation power

To install a new emitter or detector, we rotated it around the optical axis to find the orientation where the polarization of the emitted pulses aligned with the correct direction of the detection crystal, i.e., when the amplitude of the electrooptic signal was maximal.

We used the standard spintronic emitters with a single permanent magnet on top and the emitters of varying roughness with three permanent magnets, as we found that adding them improved our signal by saturating the magnetization of the ferromagnetic layer.

4.5 Raw measured data

We show representative THz waveforms and spectra in figures 4.4 (spintronic emitters, GaP detector in dry air), 4.5 (nonlinear crystal emitters, GaP detector in dry air), 4.6 (measurements with the GaP detector without dry air). All measurements are plotted as waveforms and spectra in appendix A.

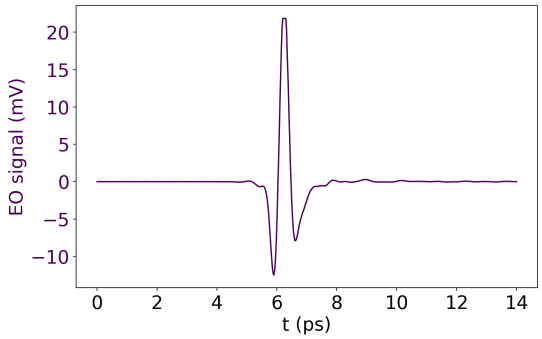

(a) 3-layer STE waveform.

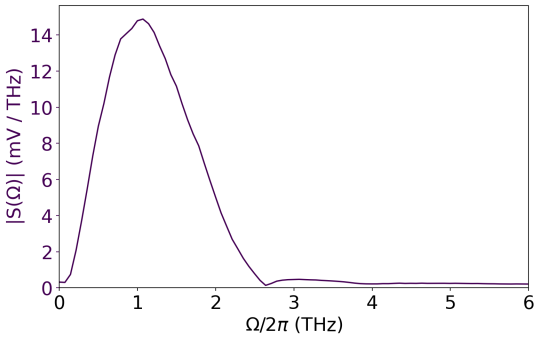

(b) 3-layer STE spectrum.

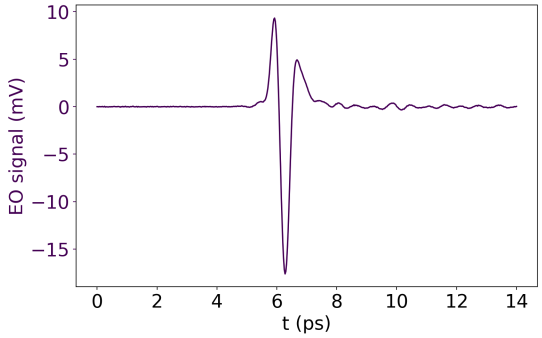

(c) 2-layer STE waveform.

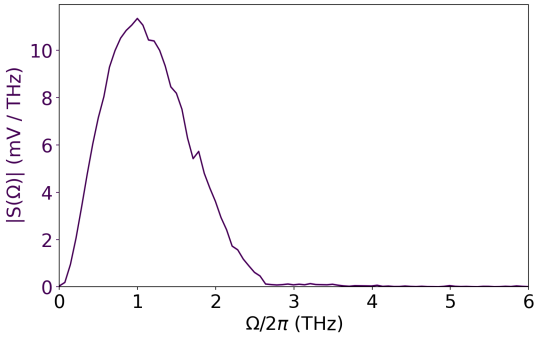

(d) 2-layer STE spectrum.

Figure 4.4 Measurements using spintronic emitters in dry air with the GaP detector. Waveforms and corresponding spectra. Note that the trilayer's spectrum continues into high frequencies, while the bilayer's spectrum is practically zero above 2.5 THz.

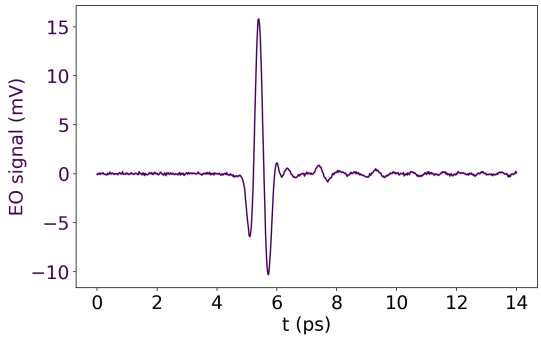

(a) ZnTe, $L = 100\,\mu\text{m}$, waveform.

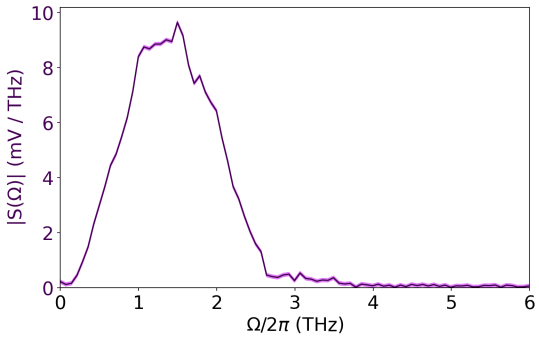

(b) ZnTe, $L = 100\,\mu\text{m}$, spectrum.

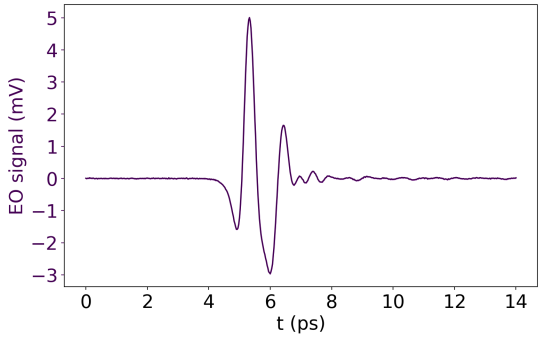

(c) ZnTe, $L = 1\,\text{mm}$, waveform.

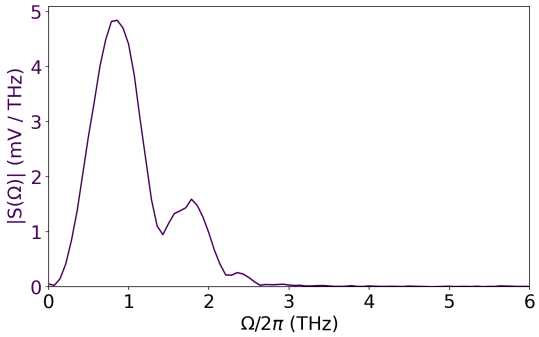

(d) ZnTe, $L = 1\,\text{mm}$, spectrum.

Figure 4.5 Reference measurements in dry air with the GaP detector. Waveforms and corresponding spectra. Note the narrower spectrum of the thick crystal with the local minimum caused by the phase mismatch.

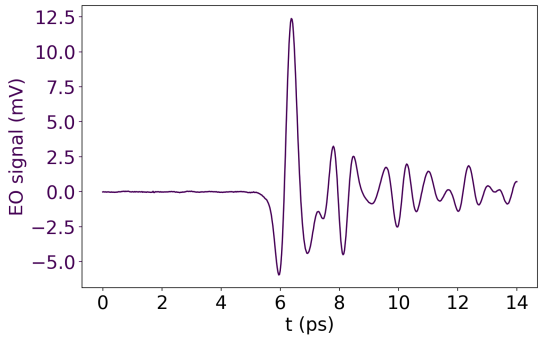

(a) 2-layer STE waveform.

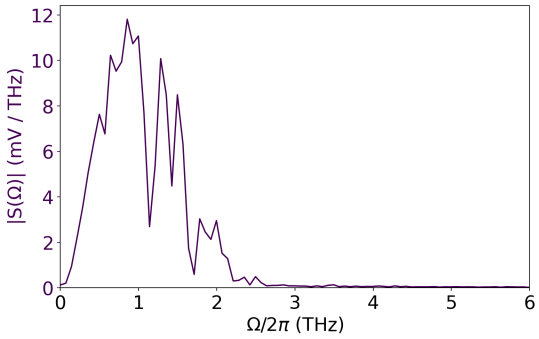

(b) 2-layer STE spectrum.

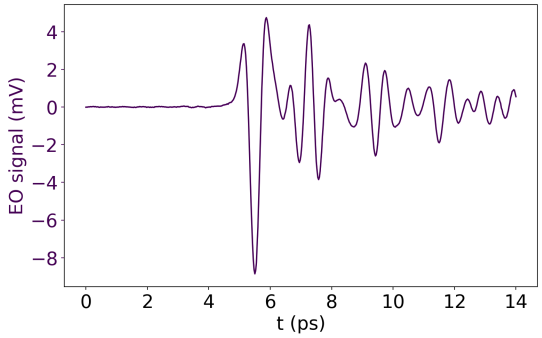

(c) ZnTe, $L = 100\,\mu\text{m}$, waveform.

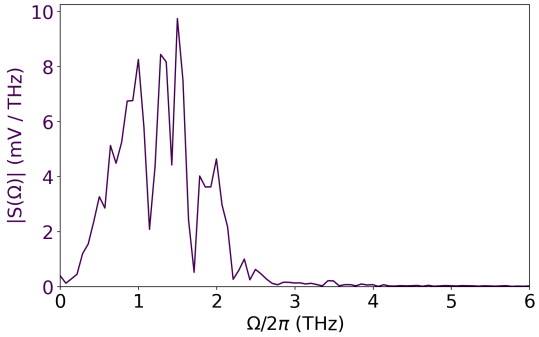

(d) ZnTe, $L = 100\,\mu\text{m}$, spectrum.

Figure 4.6 Measurements in air with water vapor with the GaP detector. Waveforms and corresponding spectra. Note the jagged shape of the spectra and the echoes visible in the waveforms.

Figure 4.7 shows data from the iris at different diameters, with $d = 5\,\text{cm}$ being a fully open iris. High-pass behavior is clearly visible, as anticipated in section 2.6.2. Figure 4.8 shows the spectra of the experimental emitters. The samples with thick gold layers absorb more radiation, so the signal from them is weaker.

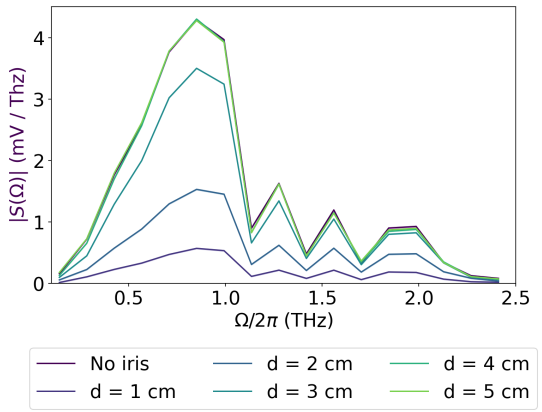

(a) The absolute value of $S(\Omega)$ for various diameters of the iris.

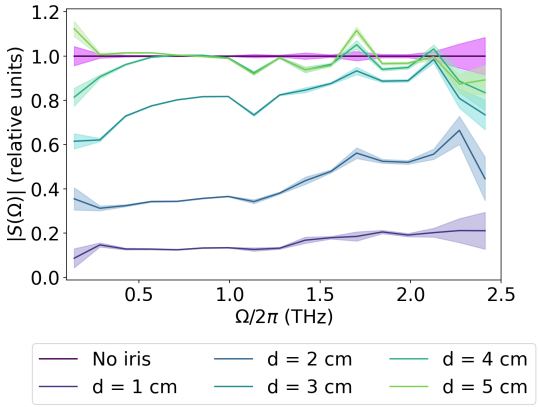

(b) Measured signal strength relative to the measurement with no iris.

Figure 4.7 Iris spectrum depending on diameter d. Note that with decreasing d, low frequencies are suppressed more than high ones. This is most clearly seen in panel (b), which shows the relative effect of closing the iris on different frequencies. Measurements were performed using the ZnTe 1 mm emitter and the GaP detector without dry air.

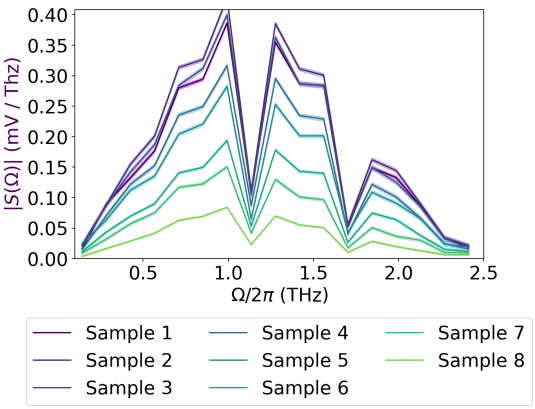

(a) The absolute value of $S(\Omega)$ for the experimental emitters.

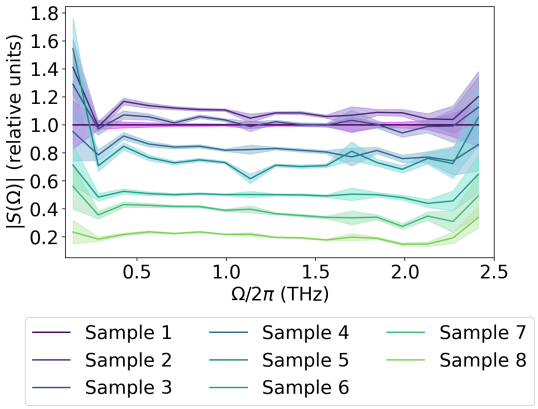

(b) Measured signal strength relative to the sample with no porous gold layer.

Figure 4.8 Spectra of experimental emitters. The thicker layers absorb more, so the signal from them is weaker.

5 Analysis and discussion

5.1 Transfer function reconstruction

For an example of the reconstruction process, see figure 5.1. This is the thinnest ZnTe reference emitter available and thus the widest unproblematic spectral range: only around 4 THz do we encounter a higher uncertainty. The setup is the GaP detector in dry air; its transfer function has a parabola-like shape terminating around 2.5 THz.

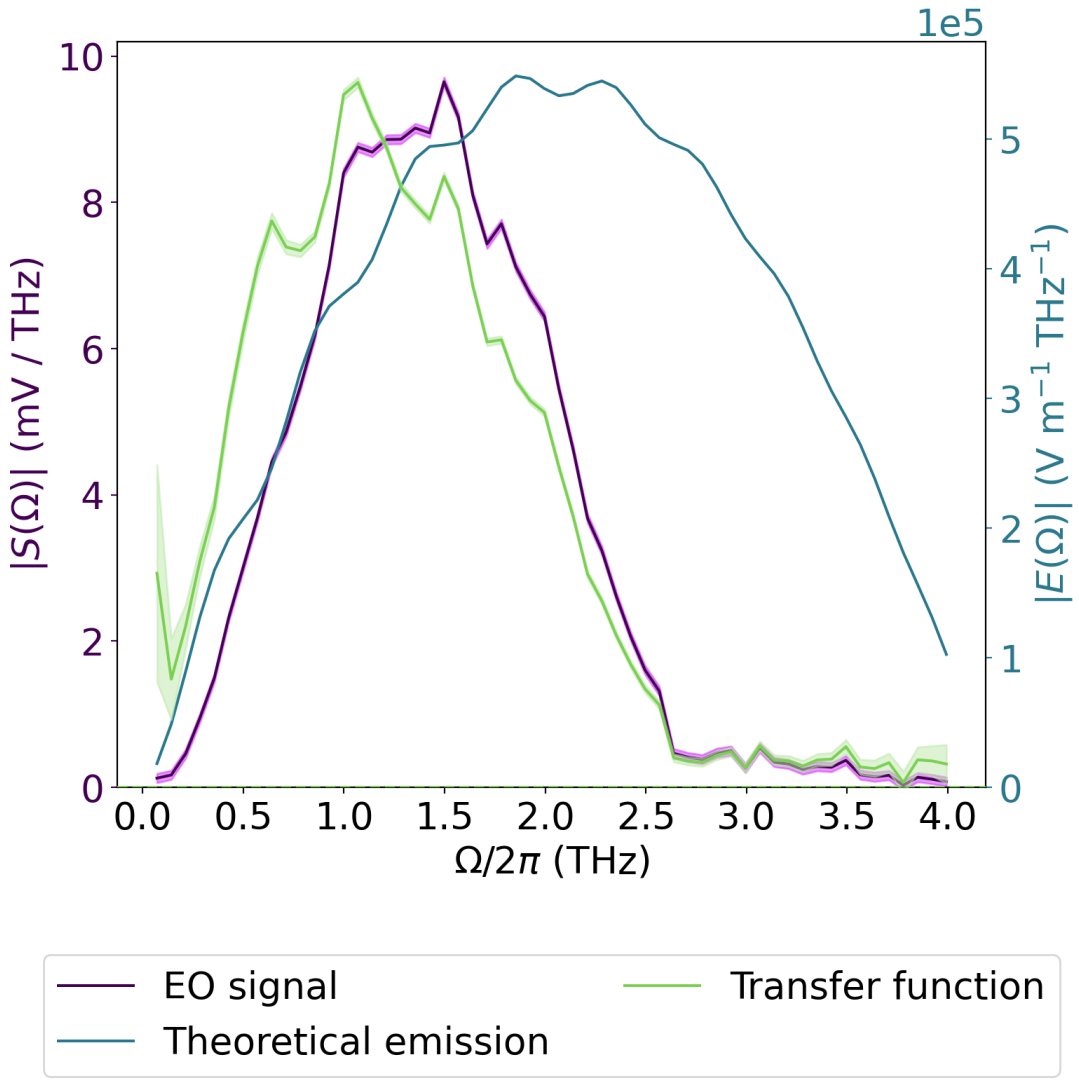

Figure 5.1 Transfer function calculation for a reference 100 µm ZnTe emitter with the GaP detector in dry air.

We use reconstructions with different emitters to illustrate possible difficulties and ways to overcome them. In this section, all reconstructions correspond to the GaP detector in dry air, and transfer functions should thus come out identical.

As anticipated in section 3.5, for thick crystals, the procedure is sensitive to the refractive index. We illustrate this for the 1 mm ZnTe emitter in figure 5.2. With the constants

from table 3.1, the first minimum of the reference does not align with the first minimum of our measurement, leading to a double peak that fails to match data from figure 5.1.

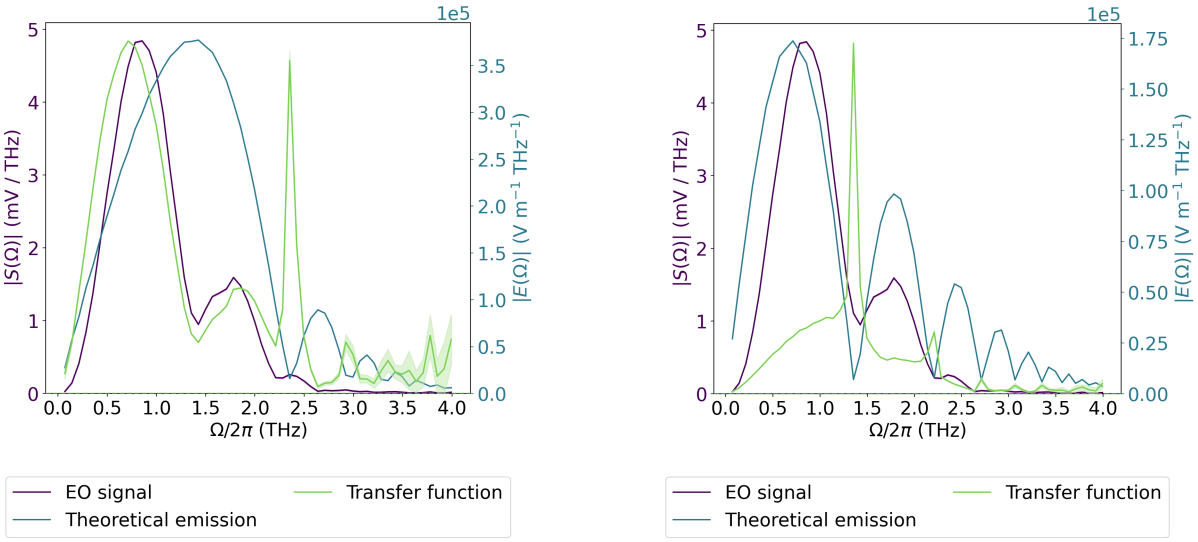

(a) Without the correction, $\varepsilon_\infty = 6.70$. The double peak of $|h(\Omega)|$ and the divergence are undesirable.

(b) With the correction, $\varepsilon_\infty = 7.42$. Away from divergences, the shape of the transfer function more closely corresponds to figure 5.1.

Figure 5.2 Transfer function calculation for a reference 1 mm ZnTe emitter with the GaP detector in dry air. The transfer function $|h(\Omega)|$ is drawn normalized to unity.

Our conclusion is that our ZnTe samples don't exactly match those described by our sources, so the values of some constants from table 3.1 may have to be modified. We have decided on a minimal intervention and only changed ε_∞. We scanned possible values between 6.30 and 7.60 and found a value where the minima of the measured signal align with the minima of the reference. The optimal value is $\varepsilon_\infty = 7.42$.

We checked the literature to find whether our changes can be explained by sample variation. The authors of Ref. [37] compare several measurements at room temperature that report values of ε_∞ between 6.0 and 6.7. This suggests that variations between samples of our order of magnitude are plausible.

Most interestingly, we note that refs. [29] and [32] disagree on ε_∞ of ZnTe by over 10%: Ref. [29] reports $\varepsilon_\infty = 6.7$, while ref. [32] reports $\varepsilon_\infty = 7.44$. Our fit almost exactly matches the latter value. However, for the $L = 500\,\mu\text{m}$ crystal, the situation is exactly the opposite, and only the value from [29] is usable, as seen in figure 5.3. For thin crystals, the procedure is less sensitive to $n(\Omega)$ and either value produces acceptable results, as seen in figure 5.4.

We also note that wherever reference emission approaches zero, $|h(\Omega)|$ has a narrow peak artifact caused by noise (as seen in figure 5.3a). We can remove these division-by-zero artifacts by averaging multiple transfer functions for the same setup.

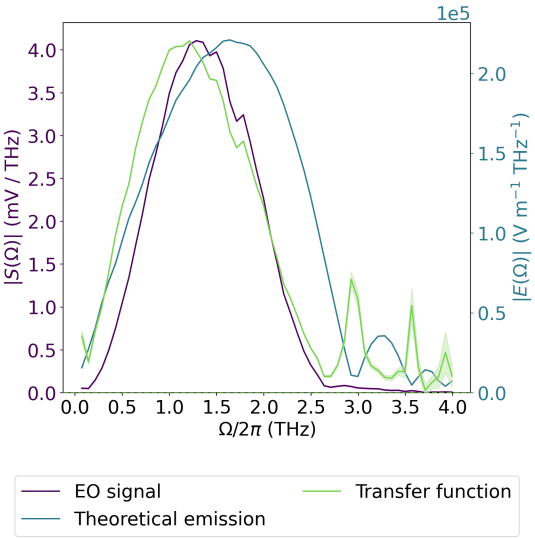

(a) Without the correction, $\varepsilon_\infty = 6.70$. The data more closely corresponds to figure 5.1.

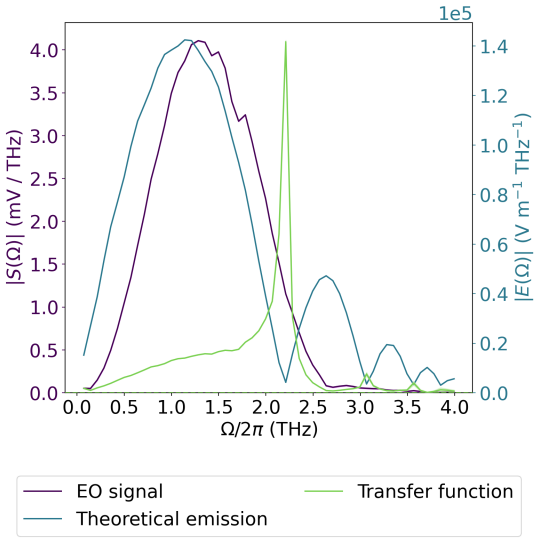

(b) With the correction, $\varepsilon_\infty = 7.42$. The divergence is unphysical.

Figure 5.3 Transfer function calculation for a reference 500 µm ZnTe emitter with the GaP detector in dry air.

As a possible explanation, we note that the refractive index is sensitive to impurities in the sample and defects caused by the manufacturing process [37]. The 500 µm and 1 mm ZnTe crystals were bought separately and thus come from different batches, or possibly even different producers.

Additionally, we note that for the 1 mm ZnTe emitter, the minimum fails to reach zero as theoretically predicted (see figure 5.2b). This means that the divergence cannot be removed entirely. One possible explanation is that the emitter is not entirely homogeneous in its refractive index, meaning that its spectrum resembles that of a sum of the two spectra in figure 3.4c. Attempts to model this would introduce additional degrees of freedom to the process, making the results harder to interpret, so we have decided to discard this reference.

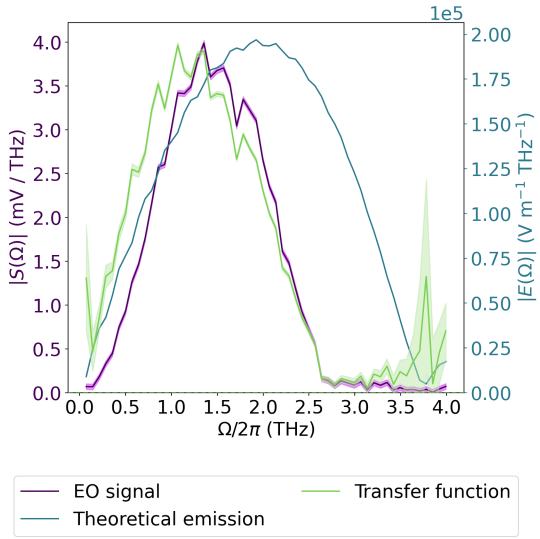

(a) Without the correction, $\varepsilon_\infty = 6.70$. ZnTe 200 µm emitter.

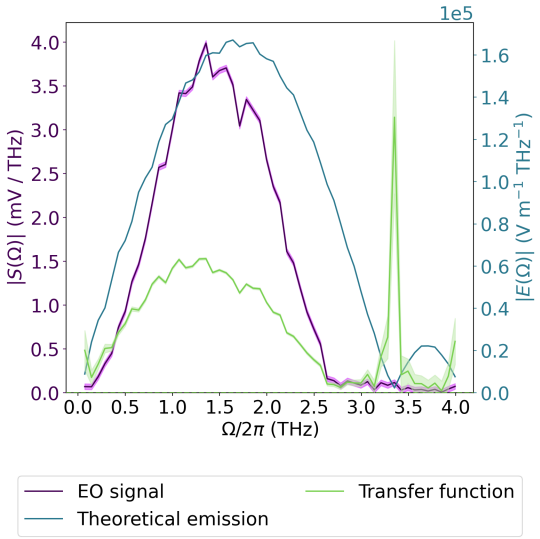

(b) With the correction, $\varepsilon_\infty = 7.42$. ZnTe 200 µm emitter.

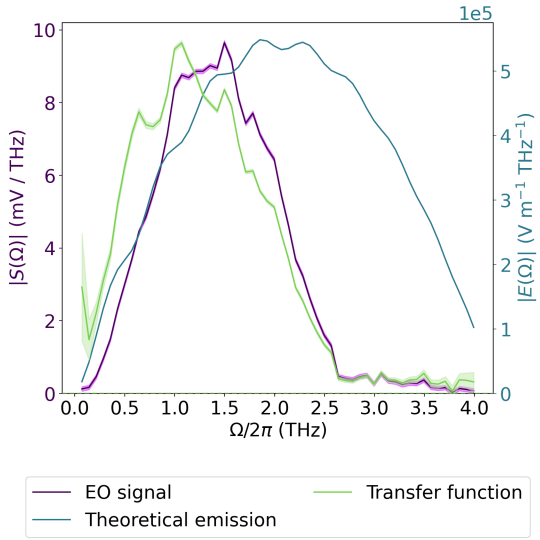

(c) Without the correction, $\varepsilon_\infty = 6.70$. ZnTe 100 µm emitter.

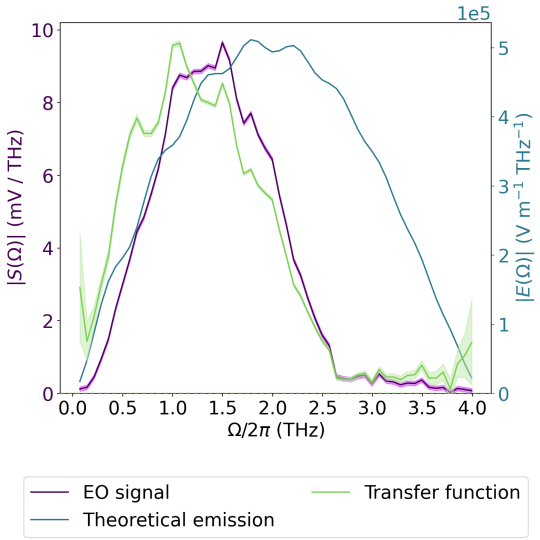

(d) With the correction, $\varepsilon_\infty = 7.42$. ZnTe 100 µm emitter.

Figure 5.4 Transfer function calculation for a reference 200 µm (panels (a), (b)) or 100 µm (panels (c), (d)) ZnTe emitter with the GaP detector in dry air. Note that even the large change in ε_∞ barely makes a visible difference.

For the GaP emitter, we have used the setup with the ZnTe 500 µm detector to find the best alignment of transfer functions with the reliable thin emitters, again using ε_∞ as the sole degree of freedom. The result is shown in figure 5.5. The resulting corrected value lies between the values in [31] and [29].

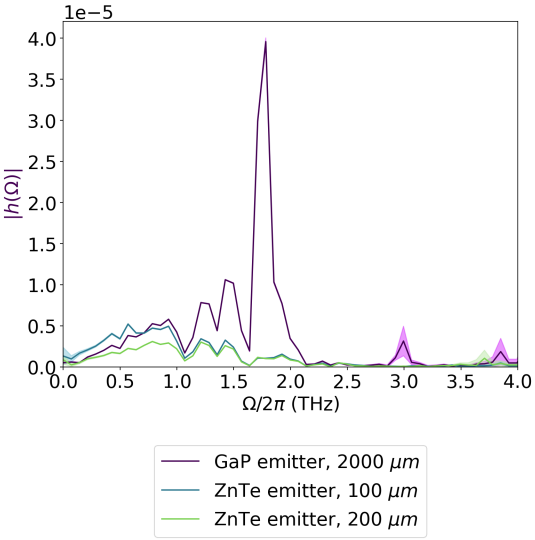

(a) Without the correction, $\varepsilon_\infty = 9.65$.

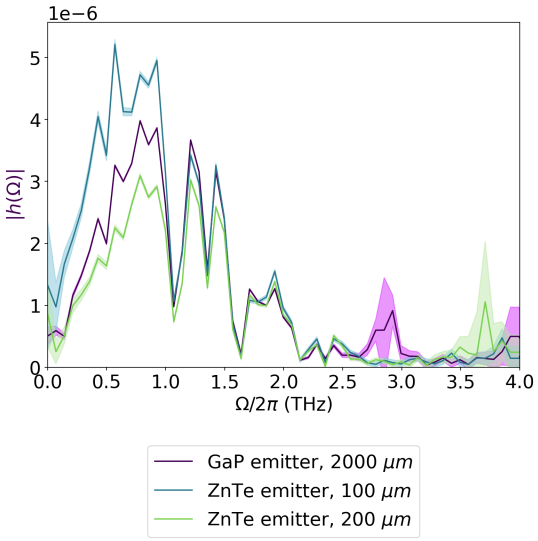

(b) With the correction, $\varepsilon_\infty = 9.40$. The transfer function found using the GaP emitter lies within the range created by the two reliable thin emitters.

Figure 5.5 Transfer function calculation for a reference 2 mm GaP emitter with a 500 µm ZnTe detector.

We note that the problems occur only for emitters with large L. For further processing, we thus use the two thinnest references: ZnTe with $L = 100\,\mu\text{m}$ and $L = 200\,\mu\text{m}$. For finding the theoretical emission, we use the value $\varepsilon_\infty = 6.70$, as reported in table 3.1. We use the lower value because it contains fewer artifacts and for consistency with the 500 µm ZnTe crystal, preferring it over the 1 mm crystal, which suffers from the shallow minimum anomaly.

5.2 Agreement between references

Having committed to our values of material parameters, we compare different reference emitters for the same setup (i.e., the same detection crystal, setup of mirrors, and experimental conditions). This serves as a verification that our method works correctly. In figure 5.6a, this is done for the measurement with the GaP detector in dry air. The references agree up to a multiplicative factor.

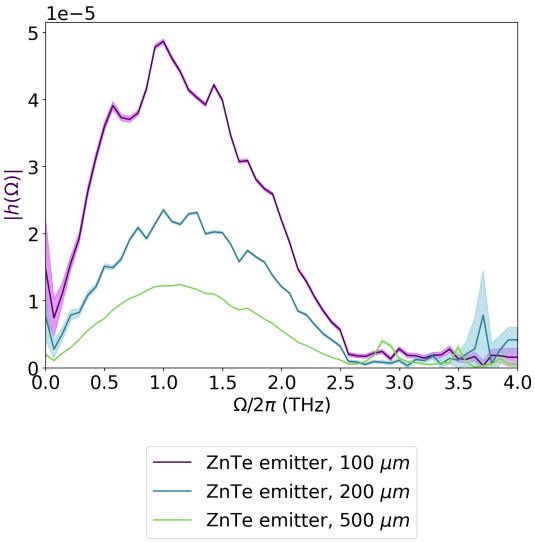

(a) The comparison obtained from raw data. The functions disagree by a multiplicative factor.

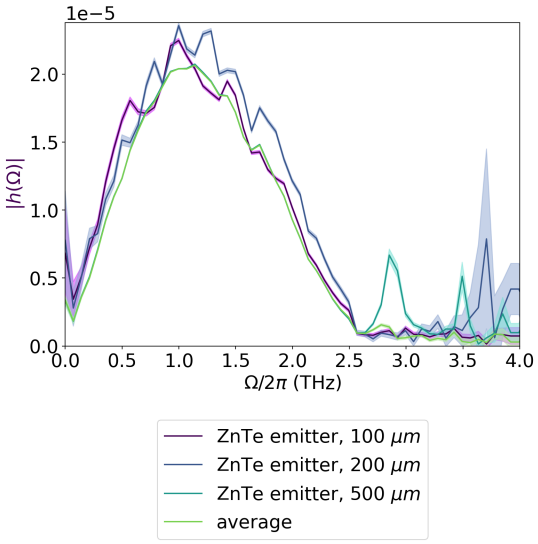

(b) The multiplicative factor has been removed. The functions have a good overlap, permitting us to use their average. Note that the average avoids the division-by-zero artifacts of the individual emitters.

Figure 5.6 The absolute value of transfer functions in the frequency domain for various reference emitters with the GaP detector in dry air.

One explanation of the discrepancy is saturation: While theoretically, the THz amplitude should scale linearly with the excitation power[1], in practice, at high powers, the conversion efficiency starts to decrease. This effect is not captured by formula (2.31), so it incorrectly appears as a part of the transfer function. However, the effect of saturation would not be this strong, as we have stopped at a point close to a 30% efficiency loss, as seen in figure 4.3.

Another possibility is that this is an effect of not finding the optimal location or orientation of the emitter. This can be verified by comparing data measured on different days with different setups. As is shown in section 5.3 below, the data in GaP measured with and without dry air has transfer functions of a comparable scale. These measurements were performed on separate days, each time requiring optimization of the setup, so any experimental mismatch would be visible. Therefore, we reject this explanation.

We note that the multiplicative factor is not random: The ratio of amplitude to excitation power is similar between emitters of different thickness (see table 4.1), while formula (2.31) says E should roughly scale with L. This leads to a multiplicative factor of roughly 5 between the 500 µm and 100 µm emitters.

Fortunately, this discrepancy does not affect our main goal, which is finding the spectral response of the detectors, and we can easily overcome it by adding a multiplicative factor to the different emitters. All further analysis is thus done with the scale of the transfer functions modified for best overlap, with the data from the 200 µm ZnTe emitter used as the reference.

The result of this change is plotted in figure 5.6b. Apart from divergences at frequencies

[1]The reason is that DFG is a second-order nonlinear process.

where the emitter does not emit, we note that the results align well. The divergences are resolved by the average: because of their correspondingly large uncertainty, they are neglected.

The frequency domain of figure 5.6b only plots the absolute value of the spectrum. We can compare the transfer functions more precisely in the time domain, which also shows information hidden in the complex phase. This is shown in figure 5.7.

We can see that the transfer functions are comparable. Their offset in the time domain is not a physical effect; it originates from the different time windows used to measure the different pulses. For further processing, we choose a reference pulse and shift the others in time for maximum overlap o with the reference, measured by the dot product:

$$o(h_1, h_2) = \int_{t_{min}}^{t_{max}} |h_1(t) h_2(t)| \, \mathrm{d}t \tag{5.1}$$

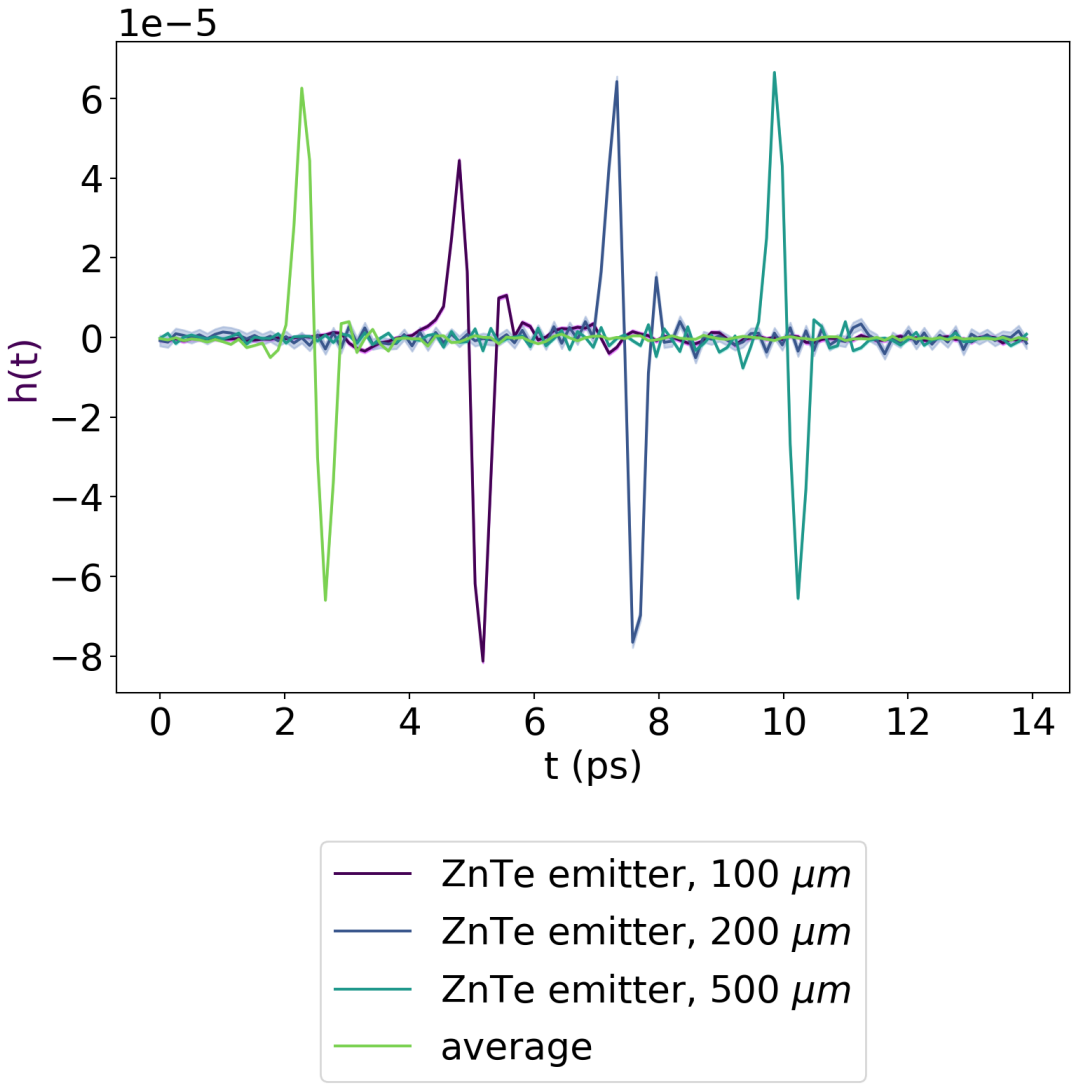

Figure 5.7 Transfer functions in the time domain for various reference emitters with the GaP detector in dry air. The offset in time is for visual clarity only.

5.3 Interpreting transfer functions

We have theoretical expectations from chapter 2.6 about how the transfer functions should be affected by well-defined changes to the setup. Our first comparison is for the GaP detector with and without dry air in figure 5.8. We compare the transfer function obtained by averaging the results using ZnTe 100, 200, and 500 µm crystals as reference emitters. In the frequency domain, water vapor absorbs certain frequencies, as anticipated in figure 2.2. We note that the same scale is used for both transfer functions and the agreement in their size is exactly as would be expected. In the time domain, the transfer function contains echoes, which are then visible in time-domain waveforms such as figure 4.6.

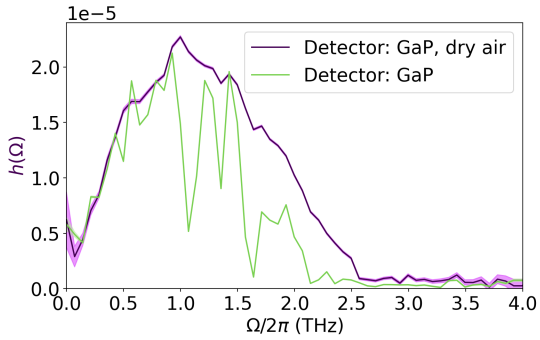

(a) Transfer functions for GaP with and without dry air in the frequency domain.

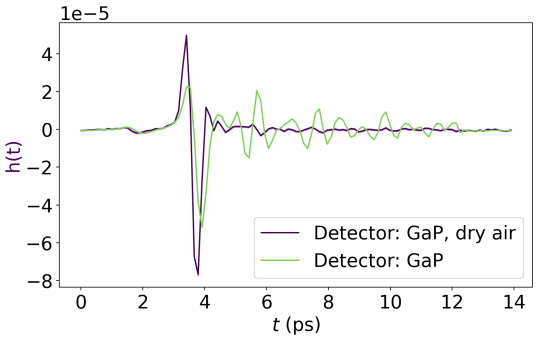

(b) Transfer functions for GaP with and without dry air in the time domain.

Figure 5.8 The effect of water vapor on the transfer function. (a) In the frequency domain, certain frequencies are lost due to absorption. (b) In the time domain, water vapor creates echoes.

The second comparison we can make with our data is between ZnTe detectors of different thickness, shown on figure 5.9. The divergence at 2.8 THz is an artifact caused by an emission minimum; we cannot remove it by averaging because we only have one reference measurement.

We see that the 500 µm emitter is sensitive over a broader frequency range, which corresponds to its broader emission. As seen theoretically in figure 3.4, the 500 µm detector has its first emission/detection around 3 THz, while for the 1 mm crystal, with the correction, the first minimum lies around 1.3 THz (see the theoretical emission spectrum in figure 5.2b).

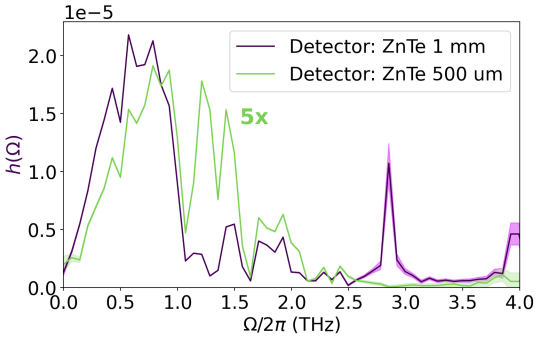

(a) Transfer functions for ZnTe detectors of different thickness. The wider detector has a narrower spectral range, but higher sensitivity within it. The data for ZnTe 500 µm is drawn at 5× magnification.

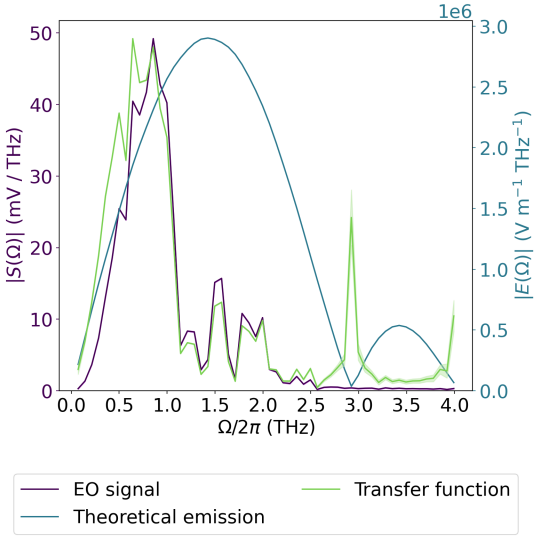

(b) The sole reconstruction for the 1 mm detector. The origin of the divergence at 2.8 THz is clearly noise.

Figure 5.9 (a) The effect of detector thickness on the transfer function. (b) The explanation of the peak at 2.8 THz.

The effect of adding an iris shutter has already been shown in part 4.5. Since we measured it using the ZnTe 1 mm reference emitter, we cannot find the transfer function for the entire setup, but we note that figure 4.7b shows the component of the transfer function due to the iris.

5.4 Spin current reconstruction

In this section, we show the results of using the transfer function to find the spectrum and pulse shape of a spin current.

5.4.1 Expectations given existing results

First, we show the results of previous work by [38], where a spin current in a 3-layer STE was reconstructed using a wider THz bandwidth. We expect our true signal to be similar to what they measure, so it is reasonable to try applying a low-pass filter to their data at the bandwidth accessible to our method to see the shape we can expect to obtain.

The results are shown in figure 5.10. Four stages can be identified in the pulse: a steep rise, determined mainly by the duration of the excitation pulse, a slower decline, a dip into the negative numbers, and a relaxation back to zero. We see that the usable spectral range makes a big difference, with 4 THz being enough to see the broad dynamics and 2.5 THz causing a significant distortion, making the pulse appear wide and symmetric.

We thus expect to see a large rise followed by a small dip, with their durations and steepness dependent of the spectral range used.

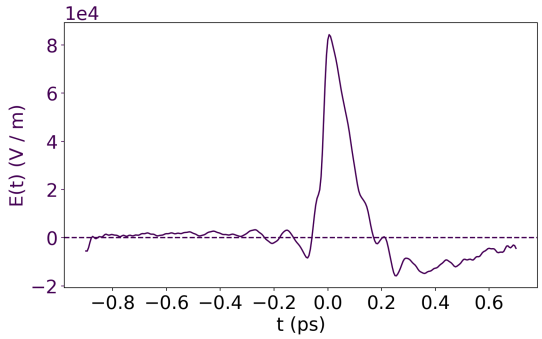

(a) The pulse as reconstructed using the full spectrum up to tens of THz.

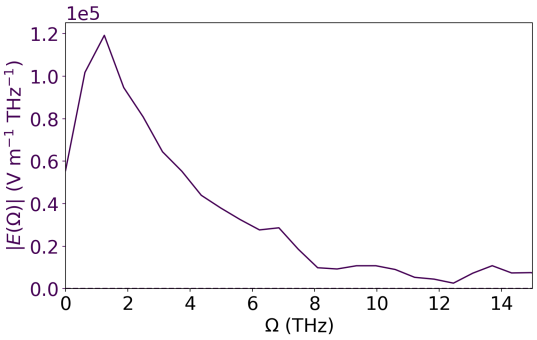

(b) The full reconstructed spectrum.

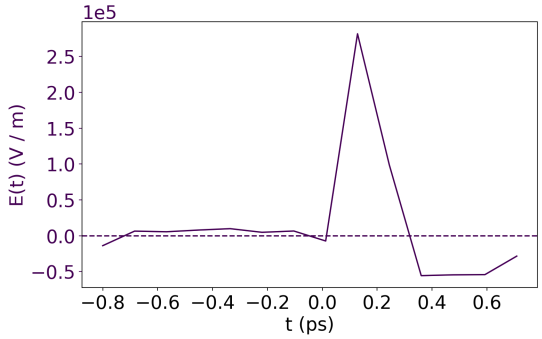

(c) The pulse with a low-pass filter cutoff at 4 THz.

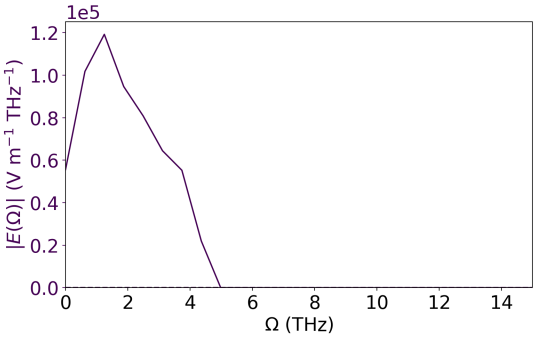

(d) The spectrum with a low-pass filter at 4 THz.

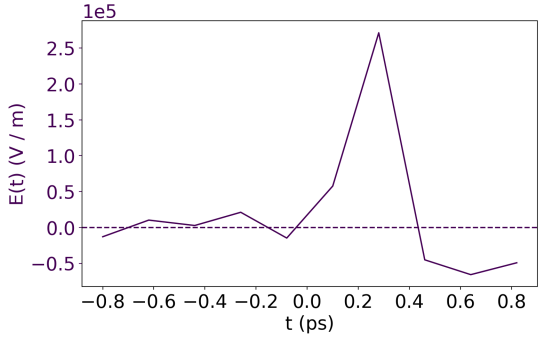

(e) The pulse with a low-pass filter cutoff at 2.5 THz.

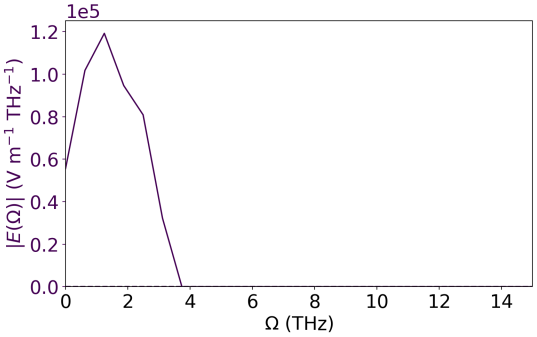

(f) The spectrum with a low-pass filter at 2.5 THz.

Figure 5.10 (a) The "true" shape of the pulse as measured using a spectrum up to tens of THz [38]. Note the asymmetry. (c) The pulse approximately as it would be seen by our method with the thinnest detector available, which might detect up to 4 THz. The pulse's broad shape is reconstructed well. (e) The pulse approximately as it may be detected with the GaP 2 mm detector, which is sensitive up to 2.5 THz. The asymmetrical shape has been washed out and the descent appears steeper than the rise. (b), (d), (f) The corresponding spectra.

5.4.2 Our reconstruction

Now we present our results. As mentioned at the end of section 5.1, we have used the average of data from the $L = 100\,\mu\text{m}$ and $L = 200\,\mu\text{m}$ ZnTe emitters, which are the most reliable ones.

We have reconstructed the currents in the 2-layer and 3-layer STE using the GaP detector with dry air (see figure 5.11) and without dry air (see figure 5.12). We can see the rapid

rise and slow return dynamics in both. The data from the bilayer appears to be almost complete, with the spectrum approaching zero for high frequencies. The trilayer, on the other hand, appears to continue into the high-frequency region where we lack sensitivity. This is consistent with the data in figure 5.10, where we see the spectrum continue being significantly nonzero in frequencies up to at least 8 THz. It is also consistent with data in figure 4.4, where we see that the measured spectrum for the 3-layer STE continues into high frequencies, while the bilayer's spectrum is practically zero above 2.5 THz.

The opposite sign of the bilayer and trilayer emission is caused by the layer order, as seen in section 4.3. The opposite sign is already visible in the waveforms in figure 4.4.

In the low-frequency region, our data is consistent with the data in figure 5.10 both in terms of the spectrum and the overall pulse shape. The beating before the first rise in the pulse is likely a numerical artifact caused by a frequency cutoff.

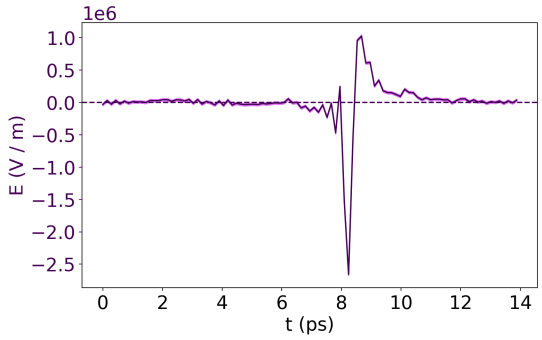

(a) Spin current in the 2-layer STE. The dynamics correspond well to our expectations.

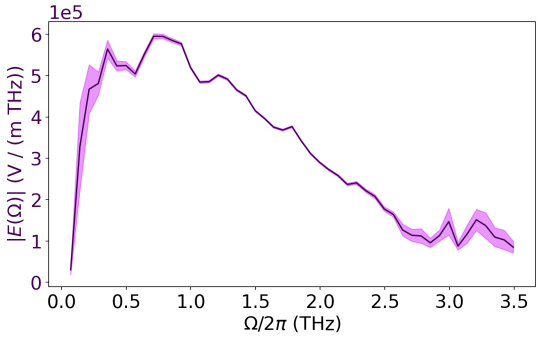

(b) Spectrum of the spin current in the 2-layer STE. Note that it dives into noise at relatively low amplitudes.

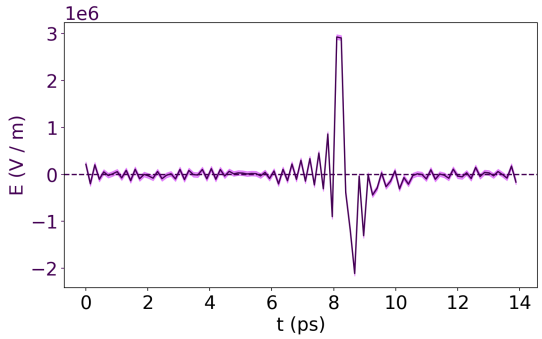

(c) Spin current in the 3-layer STE. The incomplete spectrum causes a beating artifact.

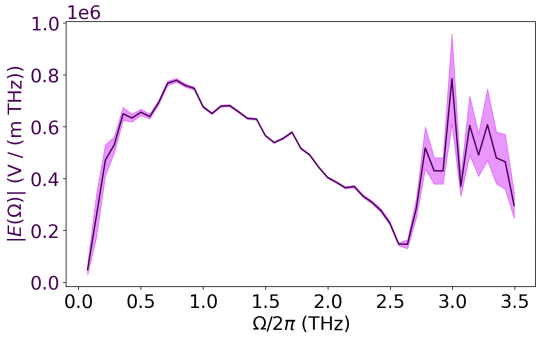

(d) Spectrum of the spin current in the 3-layer STE. Note that it appears to continue into the region where the reconstruction is less reliable.

Figure 5.11 Pulses reconstructed using the GaP detector in dry air.

The measurement without dry air shows a similar broad dynamics, but its spectrum (shown on panel 5.12a) contains peaks at frequencies where water vapor absorbs particularly well. This may be a consequence of noise, but also of the changes in humidity between measuring the reference and the STE. We conclude that spin current reconstruction is possible on data measured without dry air, as the main features are still discernible, but the resulting noise level is much higher.

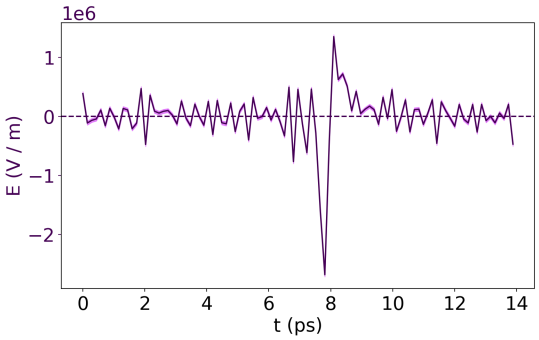

(a) Spin current in the 2-layer STE, measured with the GaP detector without dry air.

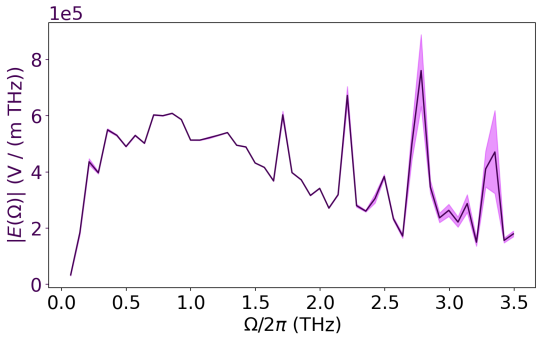

(b) Spectrum of the spin current in the 2-layer STE, measured with the GaP detector without dry air. The losses at water vapor lead to increased noise at the corresponding frequencies.

Figure 5.12 The spin current in the 2-layer STE reconstructed using the GaP detector without dry air.

5.4.3 Comparison of our data and expected data

To compare our data and the data from [38] more explicitly, we show the pulses reconstructed by either method in a single graph. We show our data (obtained with dry air) together with the unmodified pulse in figure 5.13. As can be seen, our data suggests a longer pulse duration, but otherwise agrees with existing results.

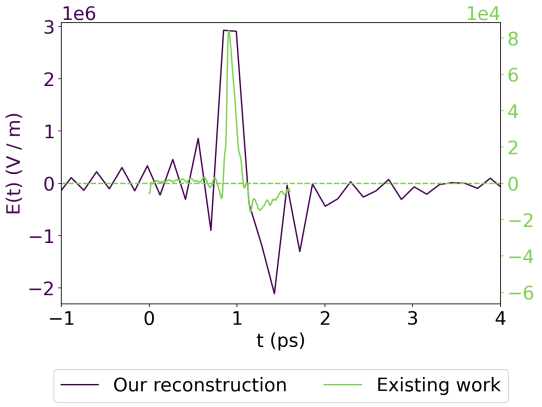

(a)

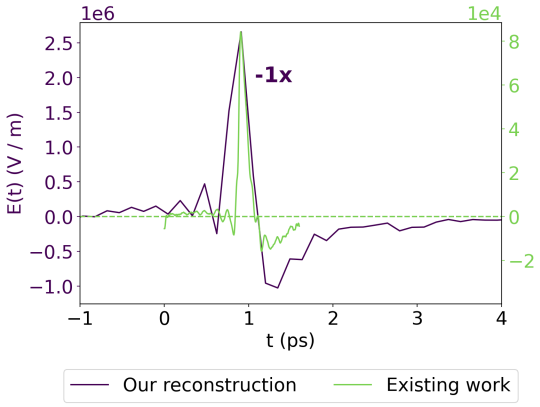

(b)

Figure 5.13 The comparison of a previously reconstructed pulse in a trilayer and our results. (a) Our 3-layer STE reconstruction compared with the exact 3-layer measurement. (b) Our 2-layer STE reconstruction compared with the exact 3-layer measurement. Our data in (b) has been multiplied by -1 for easier comparison of the shape.

To separate the effect of the different frequency bandwidths from other differences, we compare our reconstructed pulse with the pulse from [38] modified by a lowpass filter at 3.5 THz. The result is shown in figure 5.14. The results, in particular for the less noisy 2-layer STE reconstruction, now overlap satisfactorily, considering that the measurements were performed independently on different samples.

(a) Our 3-layer STE reconstruction compared with the low-pass-filtered measurement.

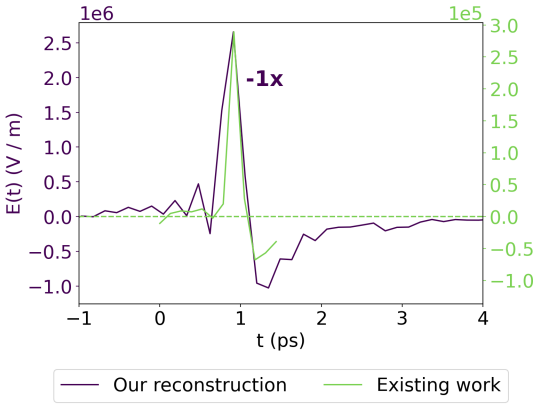

(b) Our 2-layer STE reconstruction compared with the low-pass-filtered measurement. Our data has been multiplied by −1 for easier comparison of the shape.

Figure 5.14 The comparison of a previously reconstructed pulse in a trilayer and our results. The previous-work results have been modified by a low-pass filter simulating our bandwidth limitations.

6 Outputs and further work

6.1 Achievements

We have researched the theory of emission from nonlinear crystals. Based on it, we have built a Python script through the modification of Matlab scripts used by a different team under different experimental conditions. We have added functionality for the automatic reconstruction of multiple currents measured in one setup using one or more references; we have implemented an averaging procedure that can effectively combine data from multiple references.

We have measured data from multiple emitter/detector combinations and used the script to reconstruct the transfer functions of the corresponding setups, which we then theoretically explained. We have verified that the method gives consistent results for three separate emitters (the three thinnest ZnTe crystals).

We have reconstructed the electric field emitted by spintronic emitters, proving that current experimental equipment can be used for this task, comparing our results with existing work and replicating its findings.

6.2 Conclusions

We have found the measurement procedure most useful for spin current reconstruction. The key is having complete transfer function information over as wide a bandwidth as possible. Thus, the best reference emitters are ZnTe, $L = 100\,\mu\text{m}$ and $L = 200\,\mu\text{m}$. Dry air significantly reduces noise.

The current setup is sufficient for seeing the broad characteristics of spin currents, but much more detailed information could be obtained with data from higher frequencies if the laser pulse were shortened. Widening the spectral bandwidth in the Laboratory of Optospintronics is planned for the next year.

The script developed in this thesis will become a part of the laboratory know-how, remaining applicable for any emitters studied in the future. In particular, our choice of a thick reference for the experimental emitters has precluded finding the dynamics of spin currents in them, but it is straightforward to repeat the experiment under better conditions (described above).

6.3 Possible improvements

As the data is sensitive to the refractive index $n(\Omega)$ (see figure 3.4 for a theoretical illustration and section 5.1 for the practical observation of this phenomenon), the method would be more robust if we could measure $n(\Omega)$ directly, which can be done through a simple transmission measurement [7]. The scripts could be modified to obtain $n(\Omega)$ from experimental data if desired. This would eliminate the dependence on material parameters from the literature which may not apply exactly to a particular emitter.

The behavior of thick emitters could be studied in detail using thin detection crystals with wider frequency ranges. This would let us see whether the shallow minima of figure 5.2 are a consistent phenomenon. If that were the case, it would suggest further study to determine whether they are caused by sample defects (such as refractive index inhomogeneity) or whether there are other physical phenomena at play.

We have found that thin emitters are better suited as detectors because of their wide bandwidth. We have not used the thinnest ZnTe crystals as detectors because thin crystals are less sensitive and thus require longer measurement periods, but our findings suggest that using them would improve the frequency range where we have good data. Using them in dry air can improve both overall sensitivity and coverage of the spectral range, increasing our maximal reliable frequency from around 2.5 THz to around 4 THz, which makes a difference in the characteristics of spin currents we can capture.

Some of the instabilities related to the Fourier transform can be resolved by doing the deconvolution in the time domain, as described in [18].

Achieving a high signal-to-noise ratio is helped by using a high excitation power, but this is only possible up to a certain saturation power. The saturation powers listed in table 4.4 do not follow an obvious pattern. Studying the underlying mechanisms of saturation may lead to finding ways to improve signal strength. It would also be useful to verify that saturation does not affect the emission spectrum, to make sure that this method works robustly.

Bibliography

1. Hirohata, Atsufumi; Takanashi, Koki. Future perspectives for spintronic devices. *Journal of Physics D: Applied Physics*. 2014, vol. 47, no. 19, p. 193001.
2. Hirohata, Atsufumi; Yamada, Keisuke; Nakatani, Yoshinobu; Prejbeanu, Ioan-Lucian; Diény, Bernard; Pirro, Philipp; Hillebrands, Burkard. Review on spintronics: Principles and device applications. *Journal of Magnetism and Magnetic Materials*. 2020, vol. 509, p. 166711.
3. Němec, Petr; Fiebig, Manfred; Kampfrath, Tobias; Kimel, Alexey V. Antiferromagnetic opto-spintronics. *Nature Physics*. 2018, vol. 14, no. 3, pp. 229–241.
4. Jungwirth, Tomáš; Marti, X.; Wadley, P.; Wunderlich, J. Antiferromagnetic spintronics. *Nature nanotechnology*. 2016, vol. 11, no. 3, pp. 231–241.
5. Hecht, E. *Optics*. Pearson Education, Incorporated, 2017. isbn 9780133977226.
6. Lee, Yun-Shik. *Principles of terahertz science and technology*. New York, NY: Springer, 2009. isbn 978-0-387-09539-4.
7. Dexheimer, Susan L. *Terahertz Spectroscopy: Principles and Applications*. Boca Raton: CRS Press, 2017. isbn 978-0-8493-7525-5.
8. Neu, Jens; Schmuttenmaer, Charles A. Tutorial: An introduction to terahertz time domain spectroscopy (THz-TDS). *Journal of Applied Physics*. 2018, vol. 124, no. 23.
9. Nádvorník, Lukáš. Spintronika na terahertzových vlnách. *Vesmír*. 2022, vol. 101, no. 1.
10. Žutić, Igor; Fabian, Jaroslav; Das Sarma, S. Spintronics: Fundamentals and applications. *Reviews of Modern Physics*. 2004, vol. 76, no. 2, pp. 323–410. issn 1539-0756. Available from doi: 10.1103/revmodphys.76.323.
11. Baltz, V.; Manchon, A.; Tsoi, M.; Moriyama, T.; Ono, T.; Tserkovnyak, Y. Antiferromagnetic spintronics. *Rev. Mod. Phys.* 2018, vol. 90, p. 015005. Available from doi: 10.1103/RevModPhys.90.015005.
12. Seifert, Tom S; Cheng, Liang; Wei, Zhengxing; Kampfrath, Tobias; Qi, Jingbo. Spintronic sources of ultrashort terahertz electromagnetic pulses. *Applied Physics Letters*. 2022, vol. 120, no. 18.
13. Maekawa, Sadamichi; Valenzuela, Sergio O.; Saitoh, Eiji; Kimura, Takashi. *Spin Current*. Oxford University Press, 2017. isbn 9780198787075. Available from doi: 10.1093/oso/9780198787075.001.0001.
14. Seifert, Tomáš; Jaiswal, S; Martens, U; Hannegan, J; Braun, Lukas; Maldonado, Pablo; Freimuth, F; Kronenberg, A; Henrizi, J; Radu, I, et al. Efficient metallic spintronic emitters of ultrabroadband terahertz radiation. *Nature photonics*. 2016, vol. 10, no. 7, pp. 483–488.
15. Papaioannou, Evangelos Th.; Beigang, René. THz spintronic emitters: a review on achievements and future challenges. *Nanophotonics*. 2021, vol. 10, no. 4, pp. 1243–1257. Available from doi: doi:10.1515/nanoph-2020-0563.
16. Sinova, Jairo; Valenzuela, Sergio O.; Wunderlich, J.; Back, C. H.; Jungwirth, T. Spin Hall effects. *Rev. Mod. Phys.* 2015, vol. 87, pp. 1213–1260. Available from doi: 10.1103/RevModPhys.87.1213.
17. Nádvorník, Lukáš; Borchert, Martin; Brandt, Liane; Schlitz, Richard; Mare, Koen A de; Výborný, Karel; Mertig, Ingrid; Jakob, Gerhard; Kläui, Matthias; Goennenwein, Sebastian TB, et al. Broadband terahertz probes of anisotropic

magnetoresistance disentangle extrinsic and intrinsic contributions. *Physical Review X*. 2021, vol. 11, no. 2, p. 021030.

18. Braun, L.; Nádvorník, L.; Gueckstock, O.; Seifert, T.; Wolf, M.; Kampfrath, T. An ultrafast multimeter for measuring photocurrents and voltages with 40 THz bandwidth. In preparation, unpublished.
19. Gueckstock, Oliver; Seeger, R. Lopes; Seifert, Tom Sebastian; Auffret, Stephane; Gambarelli, Serge; Kirchhof, Jan Niklas; Bolotin, Kirill I.; Baltz, Vincent; Kampfrath, Tobias; Nádvorník, Lukáš. Impact of gigahertz and terahertz transport regimes on spin propagation and conversion in the antiferromagnet IrMn. *Applied Physics Letters*. 2022, vol. 120, no. 6.
20. Rouzegar, Reza; Brandt, Liane; Nádvorník, Lukáš; Reiss, David A; Chekhov, Alexander L; Gueckstock, Oliver; In, Chihun; Wolf, Martin; Seifert, Tom S; Brouwer, Piet W, et al. Laser-induced terahertz spin transport in magnetic nanostructures arises from the same force as ultrafast demagnetization. *Physical Review B*. 2022, vol. 106, no. 14, p. 144427.
21. Jiménez-Cavero, Pilar; Gueckstock, Oliver; Nádvorník, Lukáš; Lucas, Irene; Seifert, Tom S; Wolf, Martin; Rouzegar, Reza; Brouwer, Piet W; Becker, Sven; Jakob, Gerhard, et al. Transition of laser-induced terahertz spin currents from torque-to conduction-electron-mediated transport. *Physical Review B*. 2022, vol. 105, no. 18, p. 184408.
22. Hattori, Toshiaki; Rungsawang, Rakchanok; Ohta, Keisuke; Tukamoto, Keiji. Gaussian beam analysis of temporal waveform of focused terahertz pulses. *Japanese journal of applied physics*. 2002, vol. 41, no. 8R, p. 5198.
23. Webster, J.G.; Eren, H. *Measurement, Instrumentation, and Sensors Handbook, Second Edition: Spatial, Mechanical, Thermal, and Radiation Measurement*. Taylor & Francis, 2014. Electrical Engineering Handbook Series. isbn 9781439848883.
24. Ware, M.; Peatross, J. *Physics of Light and Optics (Black & White)*. Brigham Young University, Department of Physics, 2015. isbn 9781312929272.
25. Saleh, B.E.A.; Teich, M.C. *Fundamentals of Photonics*. Wiley, 2019. Wiley Series in Pure and Applied Optics. isbn 9781118770092.
26. Vugmeyster, I. D.; Whitaker, J. F.; Merlin, R. GaP based terahertz time-domain spectrometer optimized for the 5-8 THz range. *Applied Physics Letters*. 2012, vol. 101, no. 18.
27. Riek, Claudius; Seletskiy, Denis V; Moskalenko, Andrey S; Schmidt, JF; Krauspe, Philipp; Eckart, Sebastian; Eggert, Stefan; Burkard, Guido; Leitenstorfer, Alfred. Direct sampling of electric-field vacuum fluctuations. *Science*. 2015, vol. 350, no. 6259, pp. 420–423.
28. Kampfrath, Tobias; Nötzold, Jan; Wolf, Martin. Sampling of broadband terahertz pulses with thick electro-optic crystals. *Applied physics letters*. 2007, vol. 90, no. 23.
29. Leitenstorfer, A; Hunsche, S; Shah, J; Nuss, MC; Knox, WH. Detectors and sources for ultrabroadband electro-optic sampling: Experiment and theory. *Applied physics letters*. 1999, vol. 74, no. 11, pp. 1516–1518.
30. Berozashvili, Yu; Machavariani, S.; Natsvlishvili, A.; Chirakadze, A. Dispersion of the linear electro-optic coefficients and the non-linear susceptibility in GaP. *Journal of Physics D: Applied Physics*. 1989, vol. 22, no. 5, p. 682.
31. Dietze, Daniel; Unterrainer, Karl; Darmo, Juraj. Dynamically phase-matched terahertz generation. *Optics Letters*. 2012, vol. 37, no. 6, pp. 1047–1049.

32. Gallot, Guilhem; Zhang, Jiangquan; McGowan, RW; Jeon, Tae-In; Grischkowsky, D. Measurements of the THz absorption and dispersion of ZnTe and their relevance to the electro-optic detection of THz radiation. *Applied Physics Letters*. 1999, vol. 74, no. 23, pp. 3450–3452.
33. Xue, Dongfeng; Zhang, Siyuan. Dependence of linear electro-optic coefficient on difference in the atomic sizes in zinc blende crystals. *Journal of Solid State Chemistry*. 1997, vol. 130, no. 1, pp. 54–57.
34. Marple, DTF. Refractive index of ZnSe, ZnTe, and CdTe. *Journal of Applied Physics*. 1964, vol. 35, no. 3, pp. 539–542.
35. Barlow, Roger J. Asymmetric statistical errors. In: *Statistical problems in particle physics, astrophysics and cosmology*. World Scientific, 2006, pp. 56–59.
36. Sundararajan, Duraisamy. *The discrete Fourier transform: theory, algorithms and applications*. World Scientific, 2001.
37. Li, HH. Refractive index of ZnS, ZnSe, and ZnTe and its wavelength and temperature derivatives. *Journal of physical and chemical reference data*. 1984, vol. 13, no. 1, pp. 103–150.
38. Gueckstock, Oliver; Seeger, R Lopes; Seifert, Tom Sebastian; Auffret, Stephane; Gambarelli, Serge; Kirchhof, Jan Niklas; Bolotin, Kirill I; Baltz, Vincent; Kampfrath, Tobias; Nádvorník, Lukáš. Impact of gigahertz and terahertz transport regimes on spin propagation and conversion in the antiferromagnet IrMn. *Applied Physics Letters*. 2022, vol. 120, no. 6.

A All measured data

In this appendix, we list all measurements made.

A.1 GaP detector, dry air

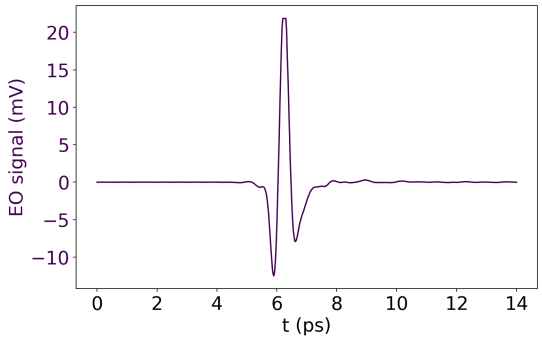

(a) THz waveform

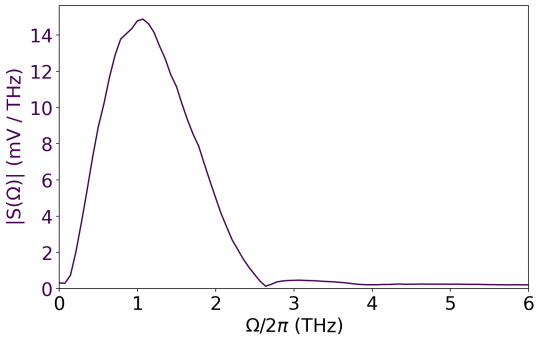

(b) Spectrum

Figure A.1 GaP detector in dry air. 3-layer STE.

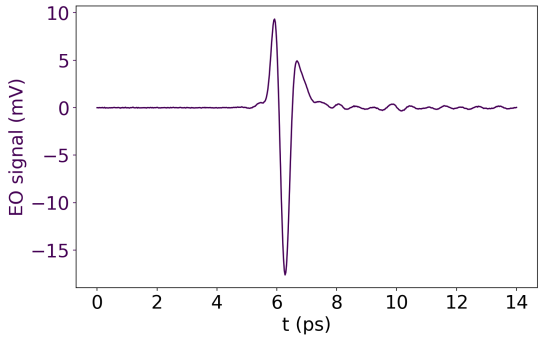

(a) THz waveform

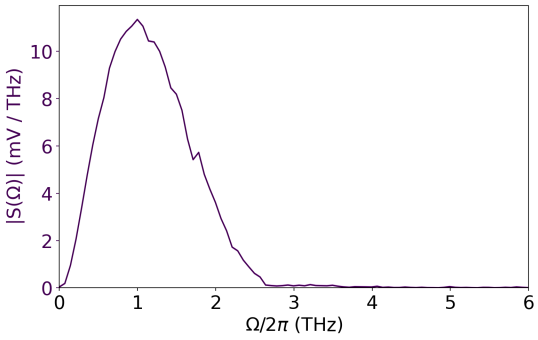

(b) Spectrum

Figure A.2 GaP detector in dry air. 2-layer STE.

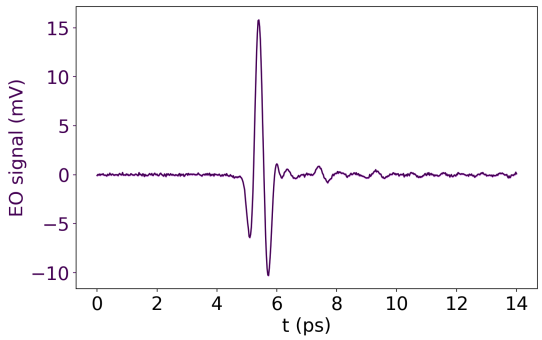

(a) THz waveform

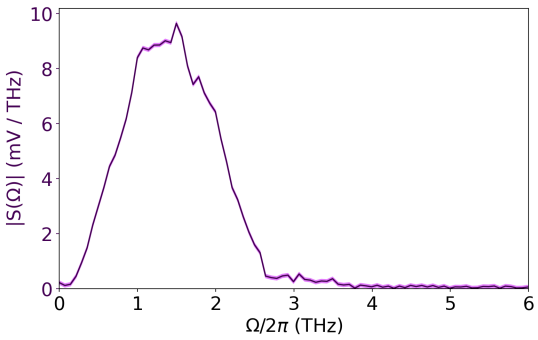

(b) Spectrum

Figure A.3 GaP detector in dry air. ZnTe 100 µm emitter.

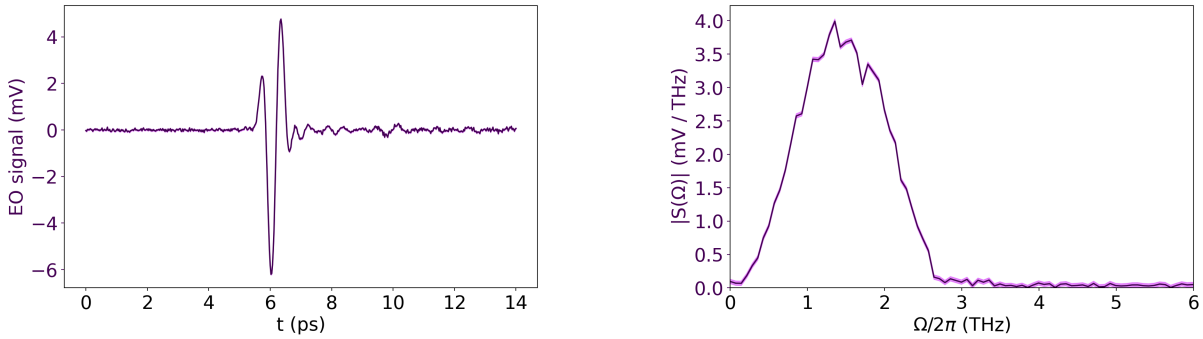

(a) THz waveform **(b)** Spectrum

Figure A.4 GaP detector in dry air. ZnTe 200 µm emitter.

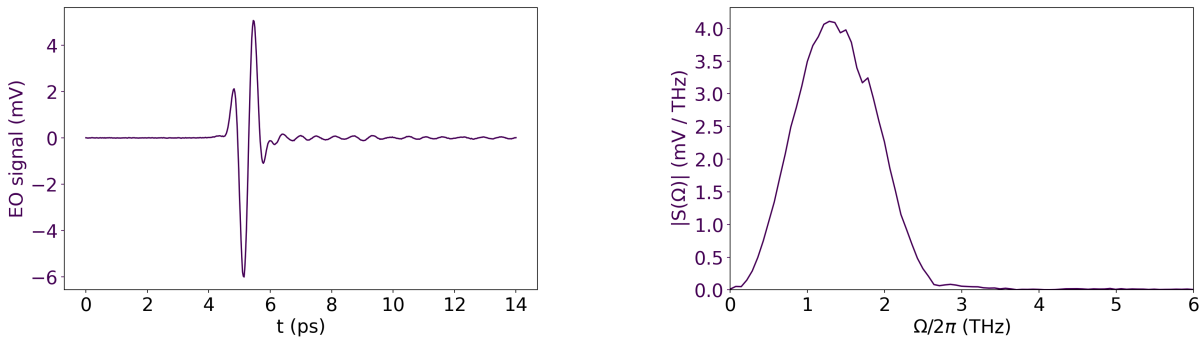

(a) THz waveform **(b)** Spectrum

Figure A.5 GaP detector in dry air. ZnTe 500 µm emitter.

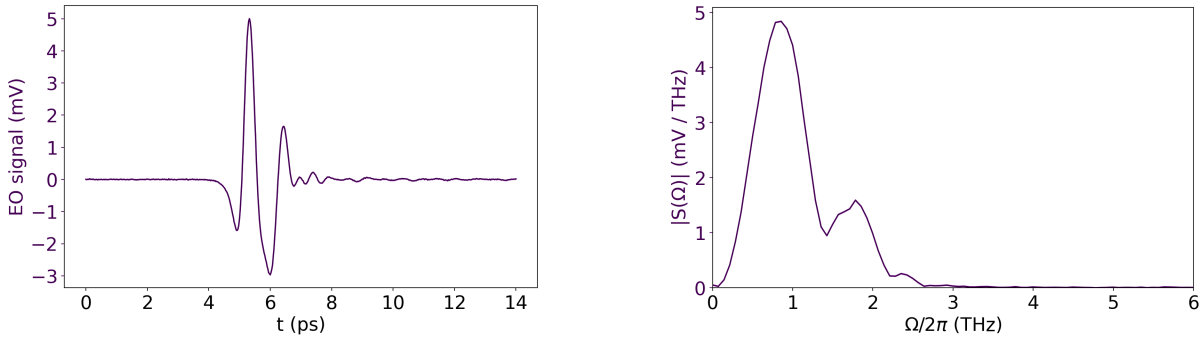

(a) THz waveform **(b)** Spectrum

Figure A.6 GaP detector in dry air. ZnTe 1 mm emitter.

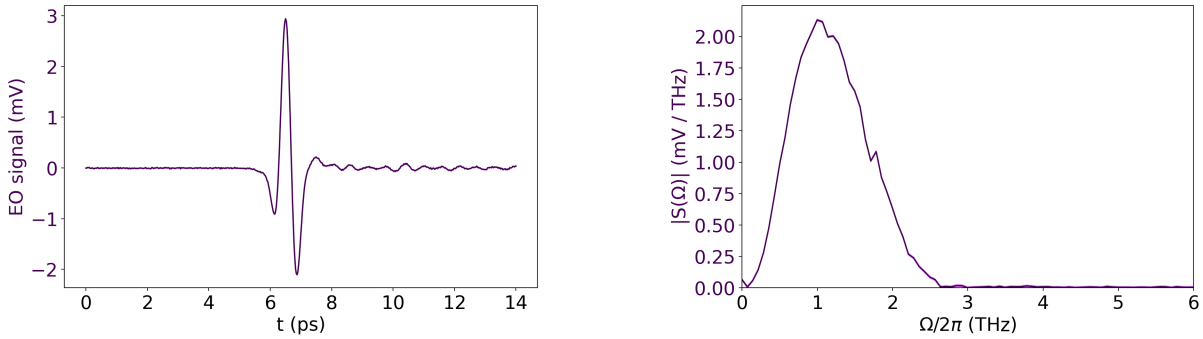

(a) THz waveform **(b)** Spectrum

Figure A.7 GaP detector in dry air. ZnTe 2 mm emitter.

A.2 GaP detector, regular atmosphere

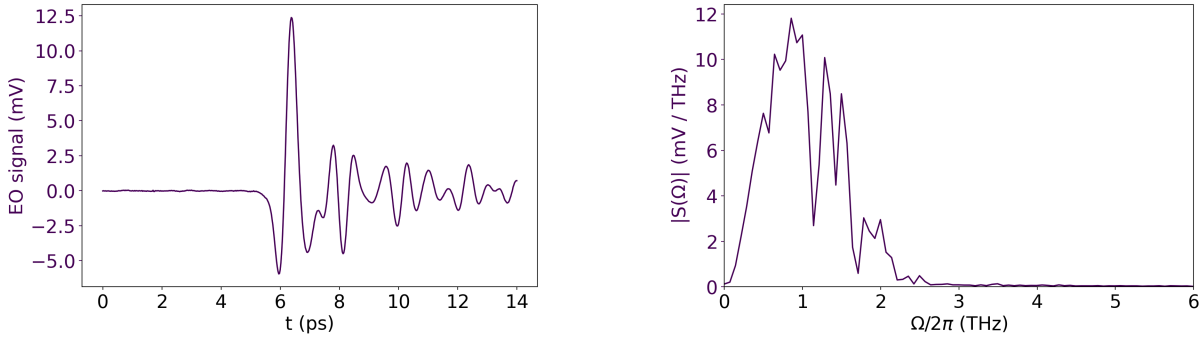

(a) THz waveform **(b)** Spectrum

Figure A.8 GaP detector. 2-layer STE.

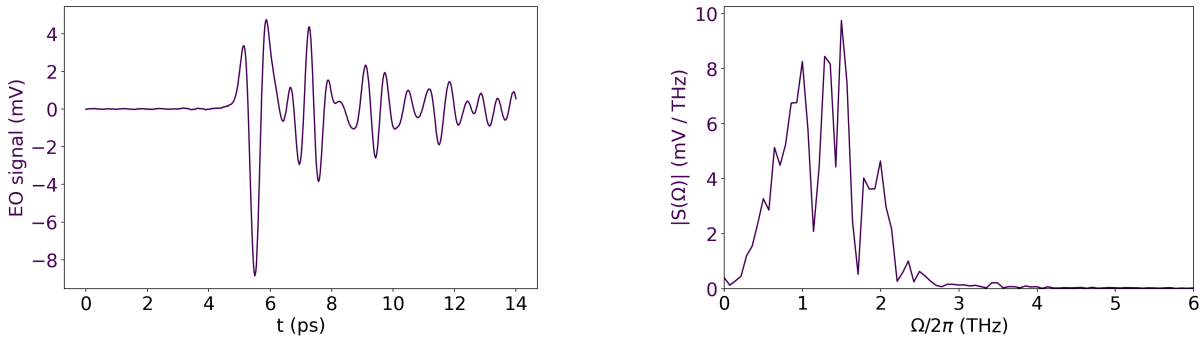

(a) THz waveform **(b)** Spectrum

Figure A.9 GaP detector. ZnTe 100 µm emitter.

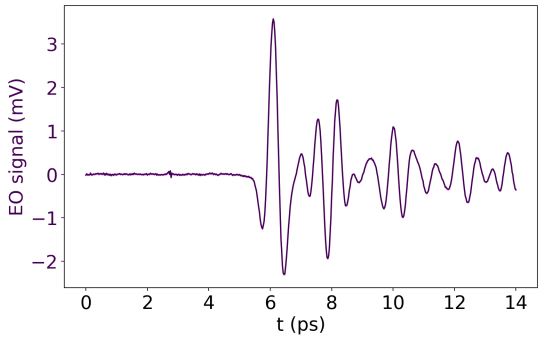

(a) THz waveform

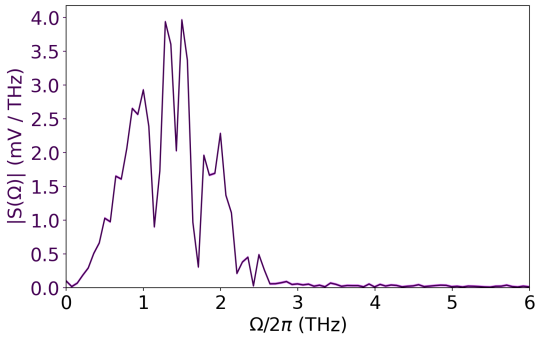

(b) Spectrum

Figure A.10 GaP detector. ZnTe 200 µm emitter.

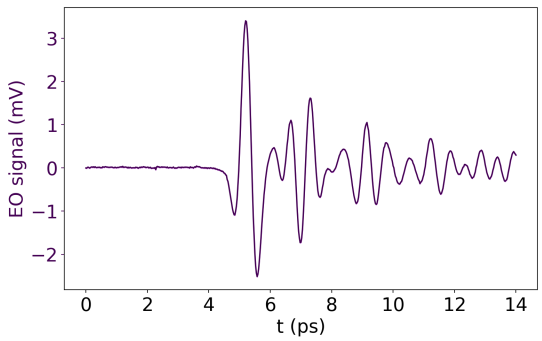

(a) THz waveform

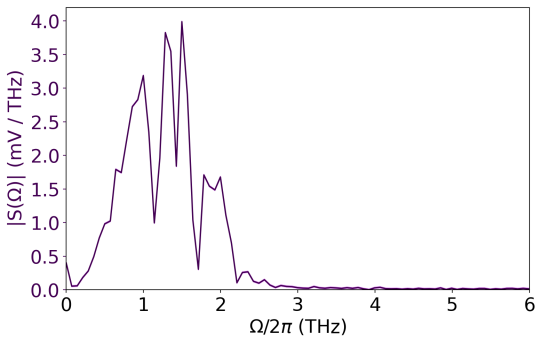

(b) Spectrum

Figure A.11 GaP detector. ZnTe 500 µm emitter.

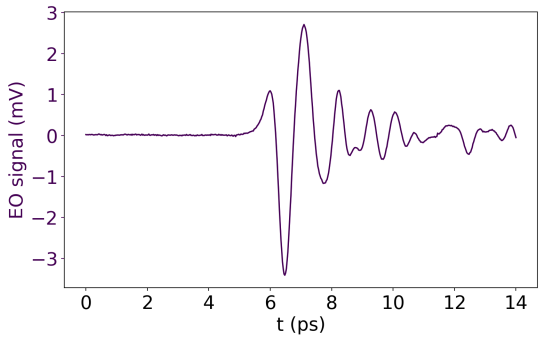

(a) THz waveform

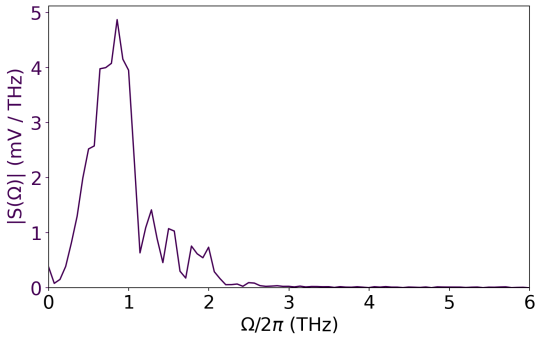

(b) Spectrum

Figure A.12 GaP detector. ZnTe 1 mm emitter.

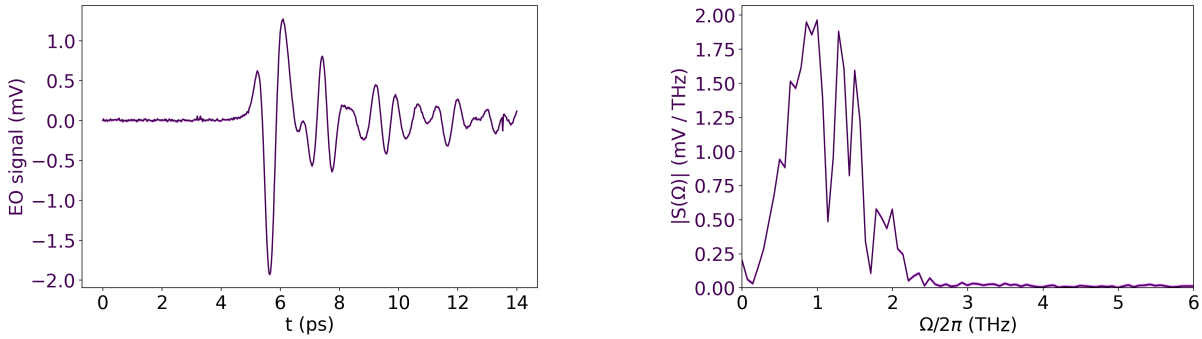

(a) THz waveform **(b)** Spectrum

Figure A.13 GaP detector. ZnTe 2 mm emitter.

A.3 ZnTe 0.5 mm detector, regular atmosphere

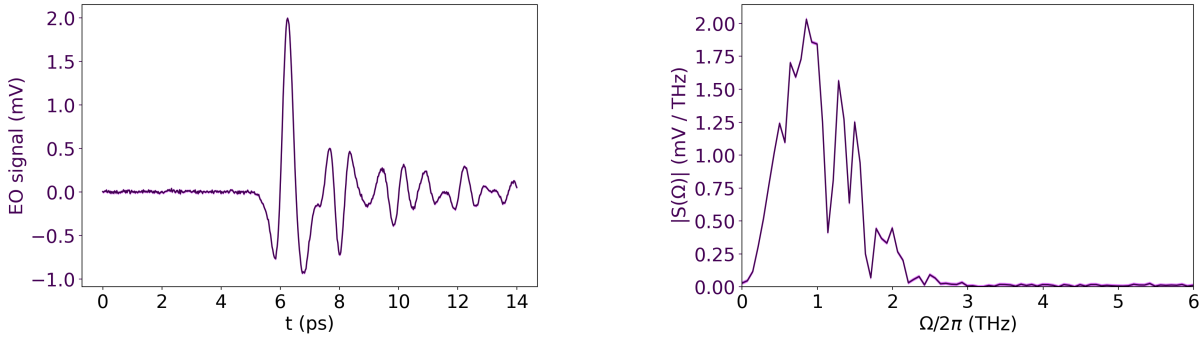

(a) THz waveform **(b)** Spectrum

Figure A.14 ZnTe 500 µm detector. 3-layer STE.

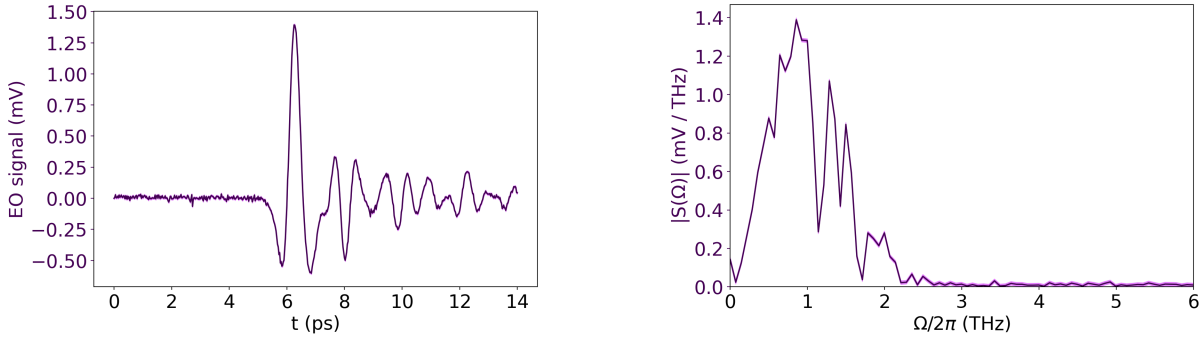

(a) THz waveform **(b)** Spectrum

Figure A.15 ZnTe 500 µm detector. 2-layer STE.

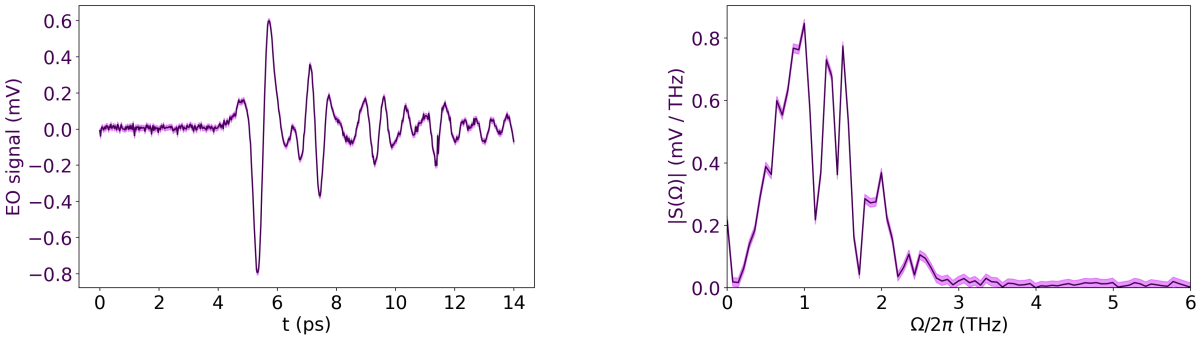

(a) THz waveform **(b)** Spectrum

Figure A.16 ZnTe 500 µm detector. ZnTe 100 µm emitter.

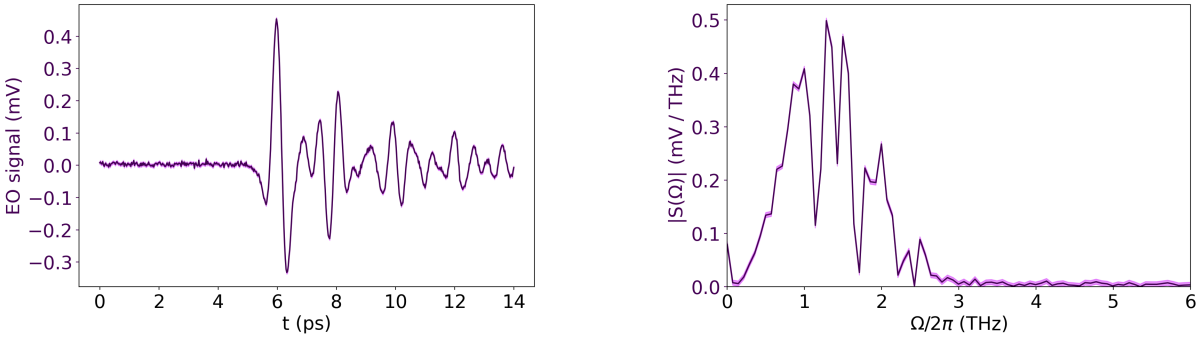

(a) THz waveform **(b)** Spectrum

Figure A.17 ZnTe 500 µm detector. ZnTe 200 µm emitter.

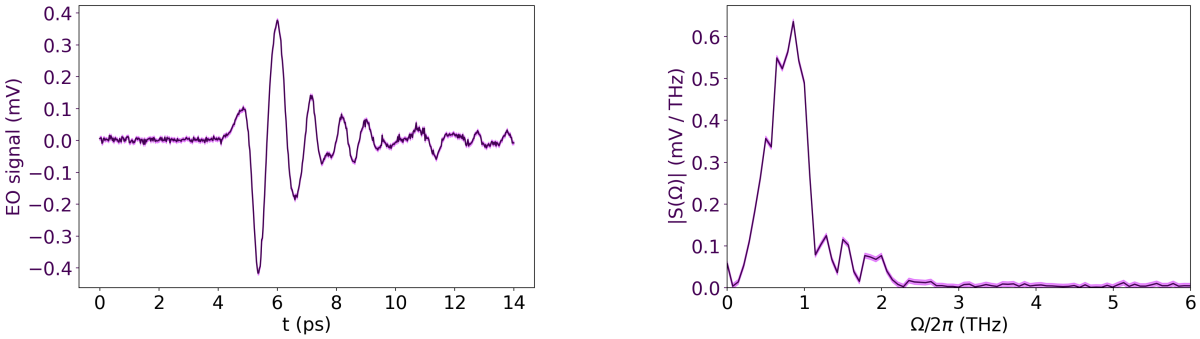

(a) THz waveform **(b)** Spectrum

Figure A.18 ZnTe 500 µm detector. ZnTe 1 mm emitter.

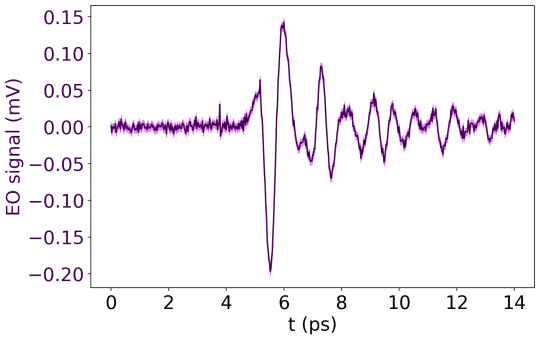

(a) THz waveform

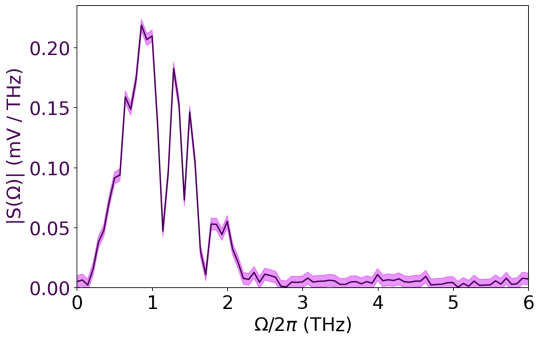

(b) Spectrum

Figure A.19 ZnTe 500 µm detector. ZnTe 2 mm emitter.

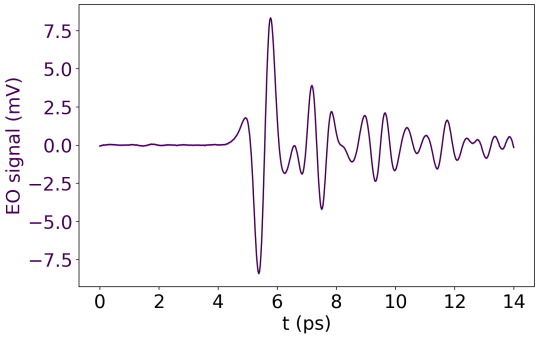

(a) THz waveform

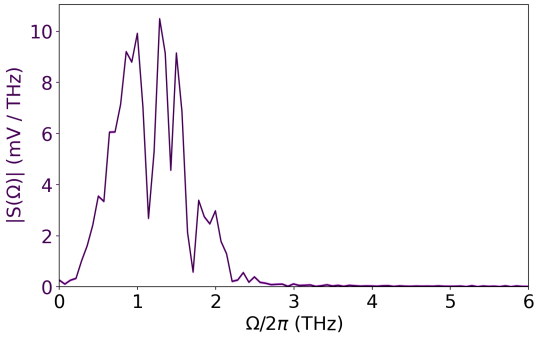

(b) Spectrum

Figure A.20 ZnTe 500 µm detector. GaP 2 mm emitter.

A.4 ZnTe 1 mm detector, regular atmosphere

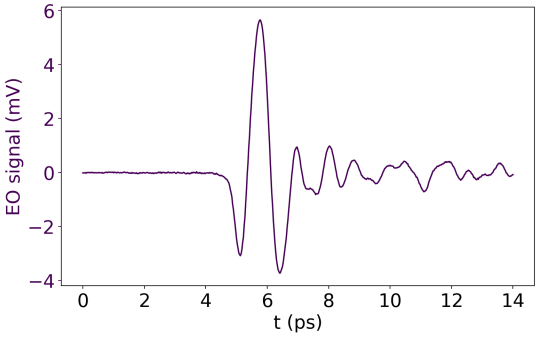

(a) THz waveform

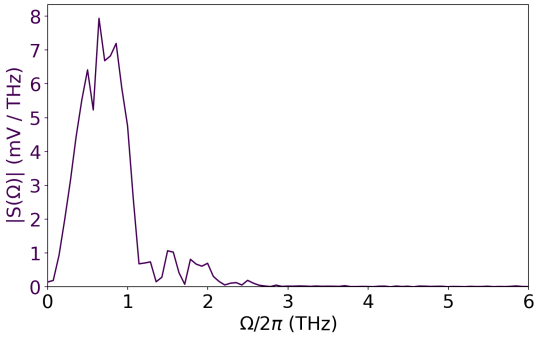

(b) Spectrum

Figure A.21 ZnTe 1 mm detector. 3-layer STE.

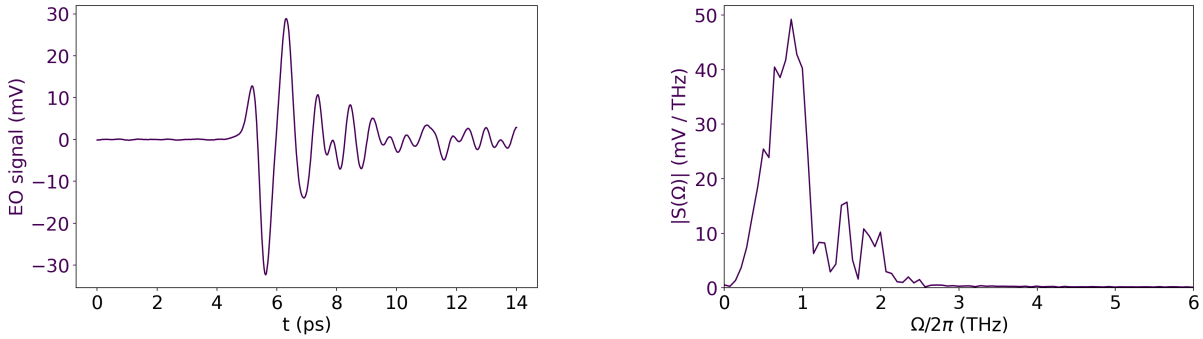

(a) THz waveform **(b)** Spectrum

Figure A.22 ZnTe 1 mm detector. GaP 2 mm emitter.

A.5 ZnTe 2 mm detector, regular atmosphere

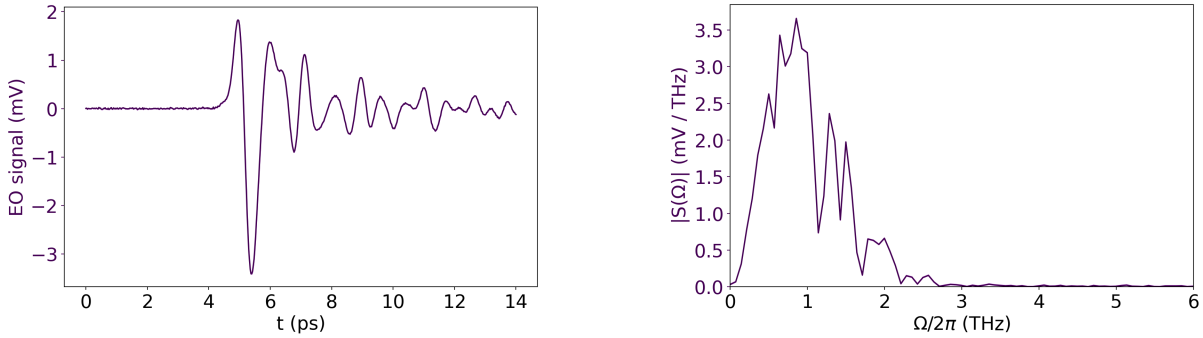

(a) THz waveform **(b)** Spectrum

Figure A.23 ZnTe 2 mm detector. 3-layer STE.

A.6 Iris shutter

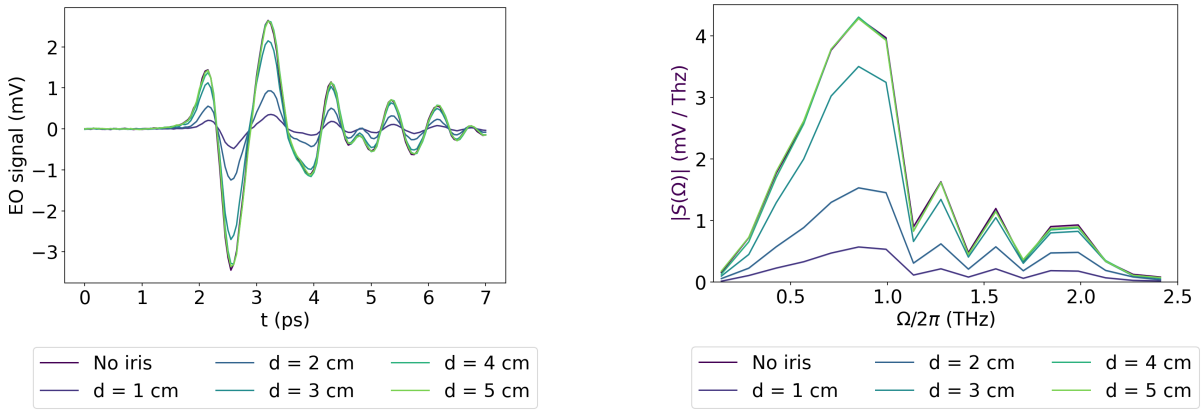

(a) THz waveforms **(b)** Spectra

Figure A.24 GaP 2 mm detector. ZnTe 1 mm emitter. Iris shutter at various diameters.

A.7 Experimental emitters

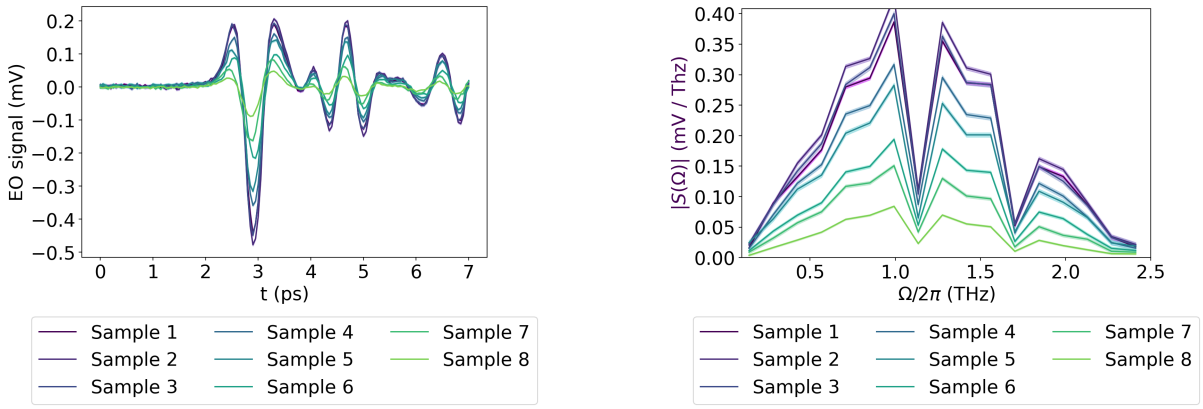

(a) THz waveforms **(b)** Spectra

Figure A.25 GaP 2 mm detector in regular atmosphere. Experimental emitters grown by Dr. Jakub Zázvorka.

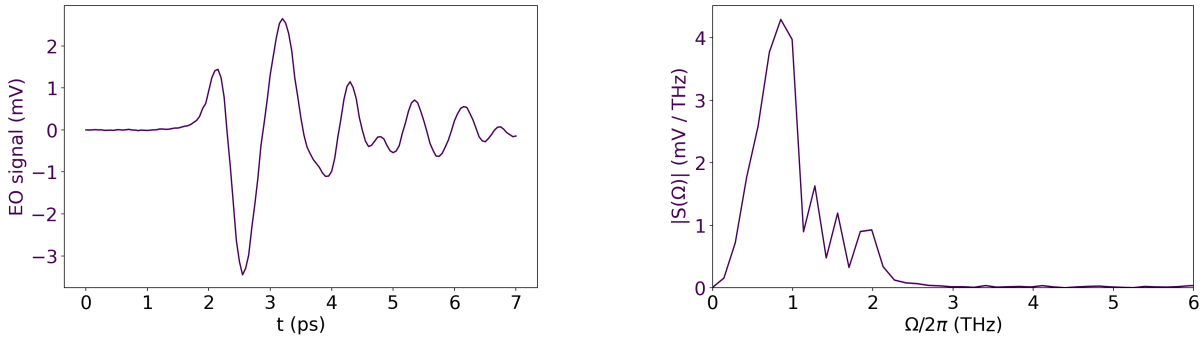

(a) THz waveforms **(b)** Spectra

Figure A.26 GaP 2 mm detector in regular atmosphere. Reference measurement with the ZnTe 1 mm emitter.